Taylor & Francis
Taylor & Francis Group

Ships and Offshore Structures

ISSN: 1744-5302 (Print) 1754-212X (Online) Journal homepage: www.tandfonline.com/journals/tsos20

Local strain response of maritime structures under accidental loading

Mohammed A. Adly & Carey L. Walters

To cite this article: Mohammed A. Adly & Carey L. Walters (06 Apr 2026): Local strain response of maritime structures under accidental loading, Ships and Offshore Structures, DOI: 10.1080/17445302.2026.2640081

To link to this article: https://doi.org/10.1080/17445302.2026.2640081

Published online: 06 Apr 2026.

SHIPS AND OFFSHORE STRUCTURES
https://doi.org/10.1080/17445302.2026.2640081

Taylor & Francis
Taylor & Francis Group

Local strain response of maritime structures under accidental loading

Mohammed A. Adly and Carey L. Walters

Department of Maritime and Transport Technology, Delft University of Technology, Delft, The Netherlands

ABSTRACT

Crashworthiness and accidental loading simulations of steel maritime structures are often performed using shell elements that might not capture the correct strain and stress localizations post-necking. This work assesses the dominant strain states appearing in such simulations. Moreover, the difference between practical shell simulations and solid simulations is analyzed by applying both elements to several realistic representative blast and impact scenarios with different material models. Strain patterns were then observed and compared between solids and shells. Generalized plane strain deformation dominated all cases where it was either imposed by geometric boundaries or transitioned to them post-necking initiation. Shells were incapable of capturing necking and strain localization reflected by solids within the plate. Results were closer for strain localization at geometric boundaries, but indicative of the role geometric details can play. Shells captured strains due to bending efficiently, but those due to membrane stresses were only captured up to necking initiation.

ARTICLE HISTORY
Received 26 August 2025
Accepted 25 February 2026

KEYWORDS
Crashworthiness; blast; thin-walled simulations; generalized plane strain; damage criteria; local analysis

1. Introduction

A major issue pertaining to crashworthiness and accidental loading simulations of maritime structures is the need to compromise the accuracy of such simulations in favor of realistic and efficient computational times. Simulations involving full maritime structures typically use shell elements (Det Norske Veritas 2010; Det Norske Veritas AS 2013; Cerik and Choung 2020; Quinton et al. 2022; Liu and Guedes Soares 2023; Prabowo et al. 2023; Suominen et al. 2024) and are expected to do so for the foreseeable future (Walters 2014; Cerik et al. 2019a; Lu et al. 2022). As many marine structures are made from ductile steel, those simulations usually involve capturing the post-necking strain localization behavior of such materials. Once strain localization occurs, the accuracy of shell element simulations is compromised (Wiegard and Ehlers 2020). Even though it is possible to circumvent this by using a necking-based failure criterion and large shell elements (Walters 2014; Pack and Mohr 2017; Cerik et al. 2020), this has an adverse effect on the simulation of post-failure propagation. The accuracy of the shell elements post-necking is compromised as the localizing portion of the material can oftentimes be smaller than the size of the practically used shell elements, and localization also introduces through-thickness stresses, which shell elements are not good at capturing. This lack of accuracy affects both plasticity and damage models. Many of the widely used phenomenological damage models, such as the Modified Mohr-Coulomb (MMC) (Bai and Wierzbicki 2010, 2008) and the Hosford-Coulomb (HC) (Mohr and Marcadet 2015), rely on both the stress triaxiality (η) and Lode angle (θ). Both η and θ require an accurate stress estimate in all principal directions, which is not available in shell elements and thus obliges the utilization of models that only depend on in-plane stress and strain parameters such as DNV RP C204:2010 (Det Norske Veritas 2010), Bressan-Williams-Hill (BWH) (Alsos et al. 2008), or plane stress assumptions applied to HC or MMC. The selection of such a model dramatically affects the results of the simulation (Coppejans and Werter 2022) in addition to the models being less accurate than models needing η and θ information. Moreover, the typical problems of mesh dependency (Liu and Guedes Soares 2023) are always present in those simulations regardless of the methods used to model plasticity and damage, because the shell element sizes used are far from the solid element sizes needed for mesh convergence.

Those challenges have led to considerable differences when various methods are utilized to try to simulate a

CONTACT Mohammed A. Adly m.a.a.m.adly@tudelft.nl Department of Maritime and Transport Technology, Delft University of Technology, Delft 2600 AA, The Netherlands

certain experimental case, such as demonstrated in the MARSTRUCT benchmark study (Ringsberg et al. 2018) or the different ISSC benchmark studies (Rizzuto et al. 2018; Quinton et al. 2022), which highlighted the effects of varying the mesh size, damage models and failure criteria on the results of a simulation, even when the same experimental description, geometry and material models are used by a team of experts. Considerable accidental loading research therefore, focuses on efforts to select the proper simulation parameters that would lead to the most accurate recreation of experiments or high fidelity simulations. The HC damage model was extended in (Pack and Mohr 2017) to introduce the Domain of Shell-to-Solid Equivalence (DSSE) which was used in works such as (Cerik et al. 2019a) to obtain relatively mesh-independent accurate results of a particular stiffened panel impact experiment. This strategy was then used in (Cerik et al. 2019b) to revisit MARSTRUCT and obtain results that follow the experiment more closely. The effect of low η ($\eta < 1/3$) on failure and its possible effect on the results of the simulation as a whole was investigated in (Kõrgesaar 2019), while (Atli-Veltin et al. 2016; Coppejans and Werter 2022) focused more on analyzing the various stress states and loading patterns present in crash cases and how they could, in turn, be affected by different simulation parameters. Even though methods such as DSSE or earlier GISMO (Neukamm et al. 2008) add fidelity by including both necking and ultimate fracture, they do not account for the multi-axial state of stress after the onset of necking. In this way, they represent the lower bound of two failure mechanisms. As shell element sizes become smaller, the deformation that happens after necking but before fracture will become increasingly important for accurate simulations, even as shell elements continue to be used.

Modeling of post-necking failure with shell elements will necessarily require a good understanding of the relationship between the behavior that can be simulated with shell elements and the multi-axial stresses that can be simulated with a converged solid mesh. To give more detail on the difference between the 3-D behavior in a solid mesh and the equivalent shell element mesh for a marine structure, a FEA simulation of a stiffened grillage will be subjected to various loading conditions with both solid elements and shell elements. There are two benefits to this strategy. First, it will highlight the exact deficiencies of the shell elements when it comes to crashworthiness and accidental loading simulations rather than just noting their sensitivity. Second, it will also clarify the strain and stress development patterns in a realistic structure subjected to various loading conditions when more accurate solid elements are used rather than the computationally efficient shell elements.

This work will therefore answer a question that has often been asked in the literature (Atli-Veltin et al. 2016; Coppejans and Werter 2022) regarding the dominant strain and stress conditions present in a realistic maritime crash or accidental loading scenario more definitely. It aims to improve upon prior work by assessing the post localization, 3-D state of stress by applying solid elements to several blast and impact conditions that are representative of realistic maritime and offshore structures. Furthermore, obtaining an exact understanding of the difference between the phenomena captured by the solid elements and shell elements would inform the research directions needed to make the shell elements as accurate as high fidelity small solid elements in large-scale crash simulations.

This paper will therefore be organized as follows. The second section will introduce the geometry of the stiffened grillage and indenters utilized for the simulations and the various loading scenarios. The third section will then introduce the material models used for the simulations. The fourth section will then present the results and discussion followed by the conclusions and suggestions for future work in section five.

2. Geometry and loading

2.1. Geometry

The geometry of the stiffened grillage used for the simulations was obtained from the 2022 version of the International Ship and Offshore Structures Congress (ISSC) Accidental Limit State (ALS) Benchmark study to determine the extent to which current FEA best practices can accurately model fracture for structures being subjected to an evolving stress state during impact (Quinton et al. 2022). To support this purpose, a series of experiments were conducted at the Memorial University of Newfoundland (MUN) on a stiffened grillage using smooth and non-smooth indenters. As of the time of writing this paper, the results of this benchmark study are yet to be published. An idealized version of the grillage as presented in (Quinton et al. 2022) is illustrated in Figure 1. Moreover, as it was also desired to study the effects of loadings directly affecting a stiffener, a new grillage design was introduced in some of the simulations with five stiffeners instead of four. This adjusted grillage is illustrated in Figure 1. A fifth stiffener now lies over the centerline of the plate, and the stiffener spacing is now 458 mm instead of 609.45 mm. A 6 mm fillet was also used between the stiffener and the plate where stress

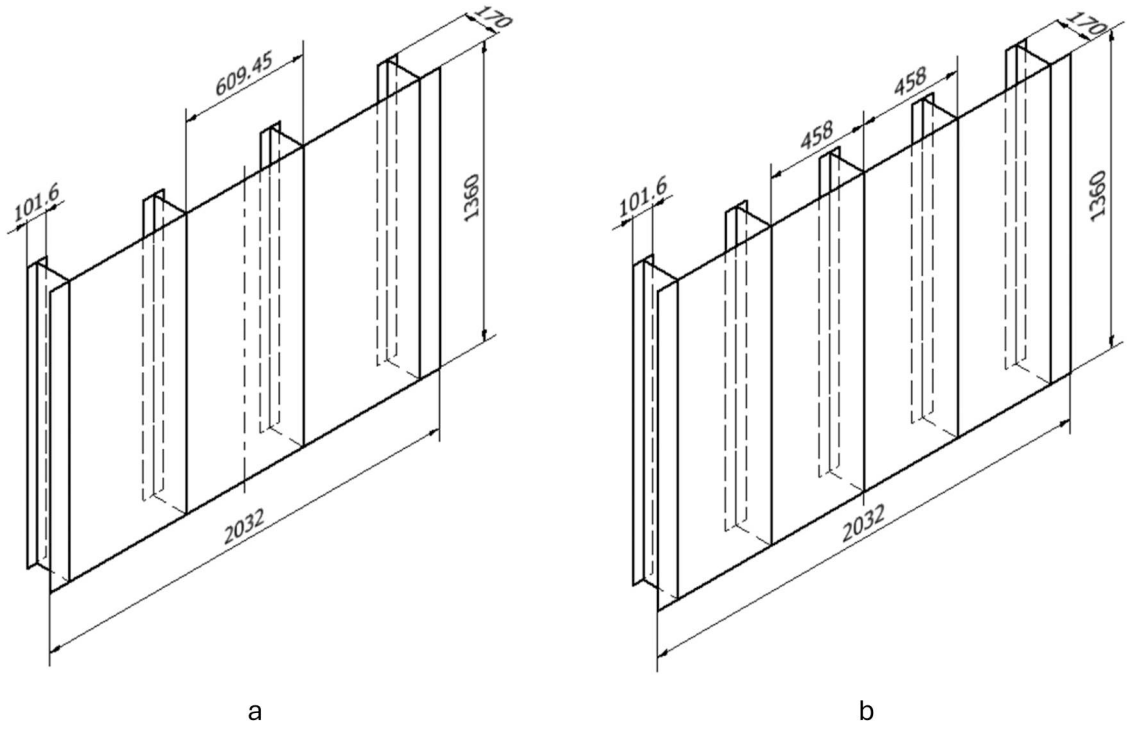

Figure 1. Grillage designs: (a) original (Quinton et al. 2022), (b) adjusted (Dimensions in mm). (This figure is available in colour online.)

concentrations are expected (the center stiffener for the adjusted grillage and the stiffener closest to the center in the original grillage). This fillet size was chosen to be commensurate with the welding codes (American Welding Society 2000) and to avoid spurious stress concentrations at the edge between the stiffener and the plate when significant bending is expected.

It should be noted that the thickness of the plate, the stiffener webs and the stiffener flanges is 7.9 mm. The stiffeners are symmetric about the centerline of the plate with the stiffener spacing held constant.

In addition to the stiffened grillage, a set of smooth indenters of three different sizes was also used in the simulations, the smallest of which was also obtained from (Quinton et al. 2022). This indenter was then scaled twice to larger versions in order to later simulate smooth indenter impacts of different sizes. The medium indenter was designed to have a diameter slightly larger than the distance between two stiffeners, and the largest indenter was designed to have a diameter slightly less than the width of the full plate (or the full extension of the longitudinal stiffeners). All three indenters were shown in Figure 2.

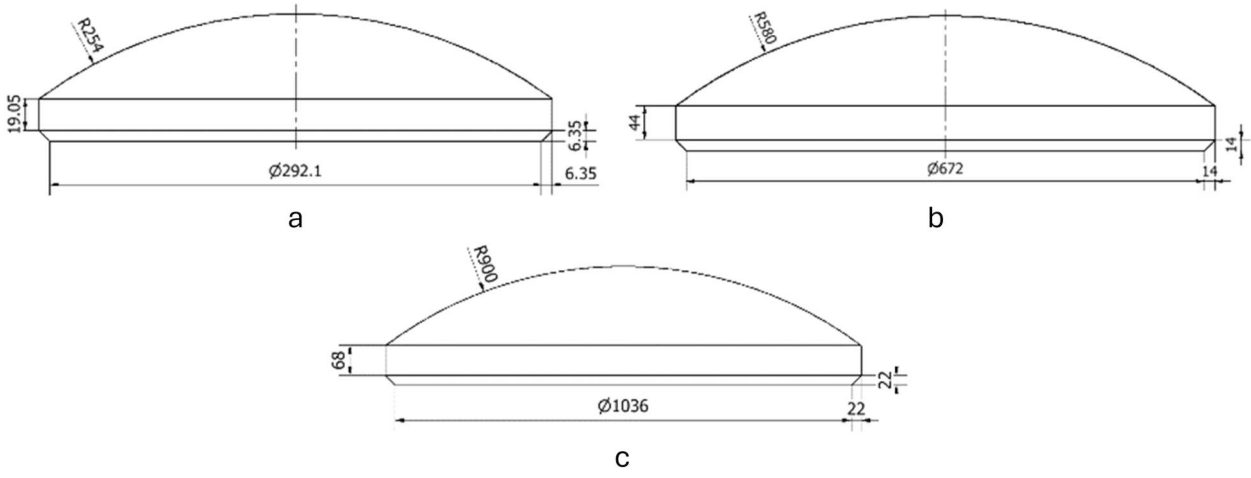

Figure 2. Smooth indenters: (a) small (Quinton et al. 2022), (b) medium, (c) large (Dimensions in mm). (This figure is available in colour online.)

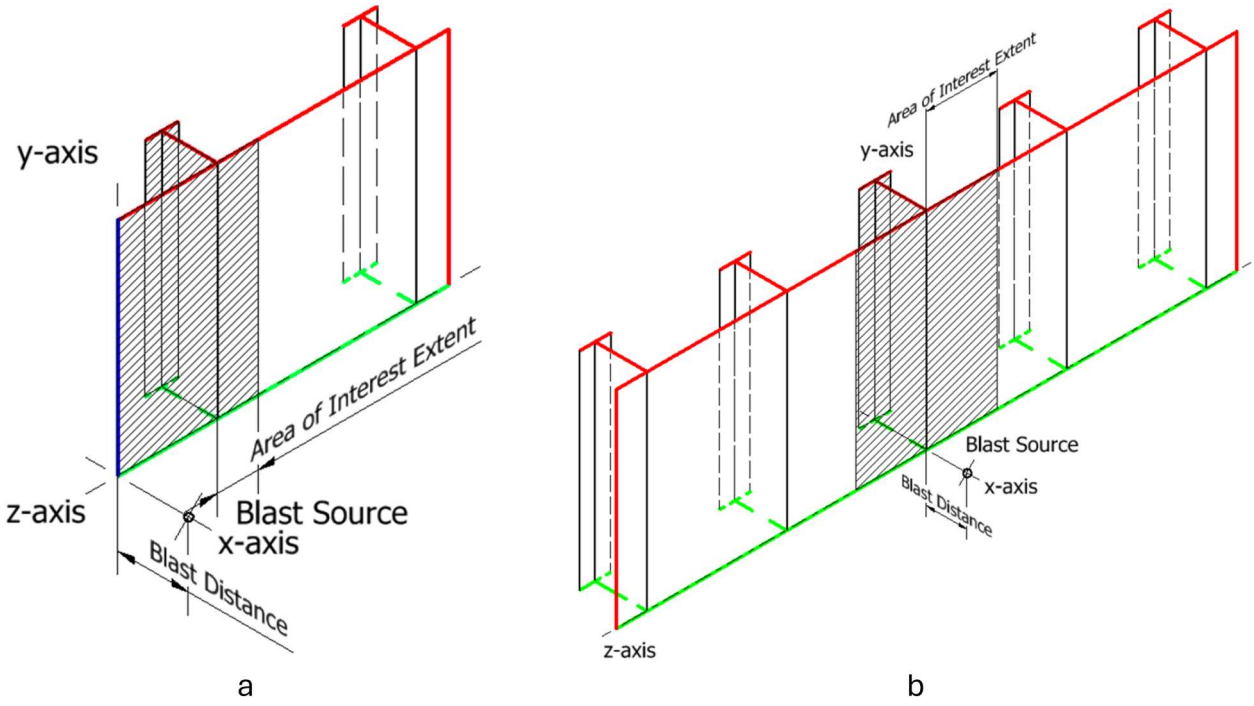

Figure 3. Blast loading setups: (a) original grillage, (b) adjusted grillage. Blue and green represent symmetry; red represents fixed boundary conditions; the hatching indicates refined mesh. (This figure is available in colour online.)

2.2. Finite element modeling parameters

For the shell element simulations, the elements were 4-noded shells with reduced integration, hourglass control, and finite membrane stresses (S4R). The shell elements had five integration points through the thickness, and the Simpson thickness integration rule was used. The characteristic dimension of those elements was uniformly set to approximately be equal to the thickness of the plate.

For the solid element simulations, two types of elements were used. In the immediate vicinity of the filleted joint between the plate and the stiffener, 8-noded linear incompatible mode brick elements were used (C3D8I), while everywhere else, 8-noded linear brick elements with reduced integration and hourglass control (C3D8R) were used. The incompatible mode elements around the filleted joint were used as they better capture behavior when extreme bending is expected. The solid simulations featured solid elements of two different characteristic dimensions. Solid elements of a characteristic dimension of almost 1/8th the thickness of the plate were used in the area of interest, where most of the significant strains are expected to occur in the grillage. Even though the solid elements would not be of sufficient density to capture the mesh convergent strains and stresses (20 elements across the half-thickness were observed to be needed for mesh convergence in small-scale plane strain simulations and only 8 across the thickness will be utilized in this work), they would be of sufficient density to capture the strain and stress development patterns and highlight the differences from the shell elements. Outside the area of interest, solid elements of a characteristic dimension approximately half the thickness of the plate were used as significant strains were not expected.

Both the shell and solid simulations were run using dynamic explicit solvers with no mass scaling or time scaling to guarantee the accuracy of the results and avoid the complexities that could arise from using either of them. The time increment was different for each simulation to guarantee stability. The Abaqus (Abaqus 2021hf9) (Dassault Systemes Simulia 2021) preset parameters for the linear bulk viscosity parameter (0.06) and the quadratic bulk viscosity parameter (1.2) were held constant.

Table 1. Blast loading scenarios

Scenario	Grillage	Symmetry condition	Blast location	Blast source (*kg* of equivalent TNT)	Blast distance (*mm*)	Area of interest extent (*mm*)
1	original	quarter	unsupported	9.8	217	125.9
2	original	quarter	whole grillage	800	3819	all
3	adjusted	half	stiffener	2	132	232

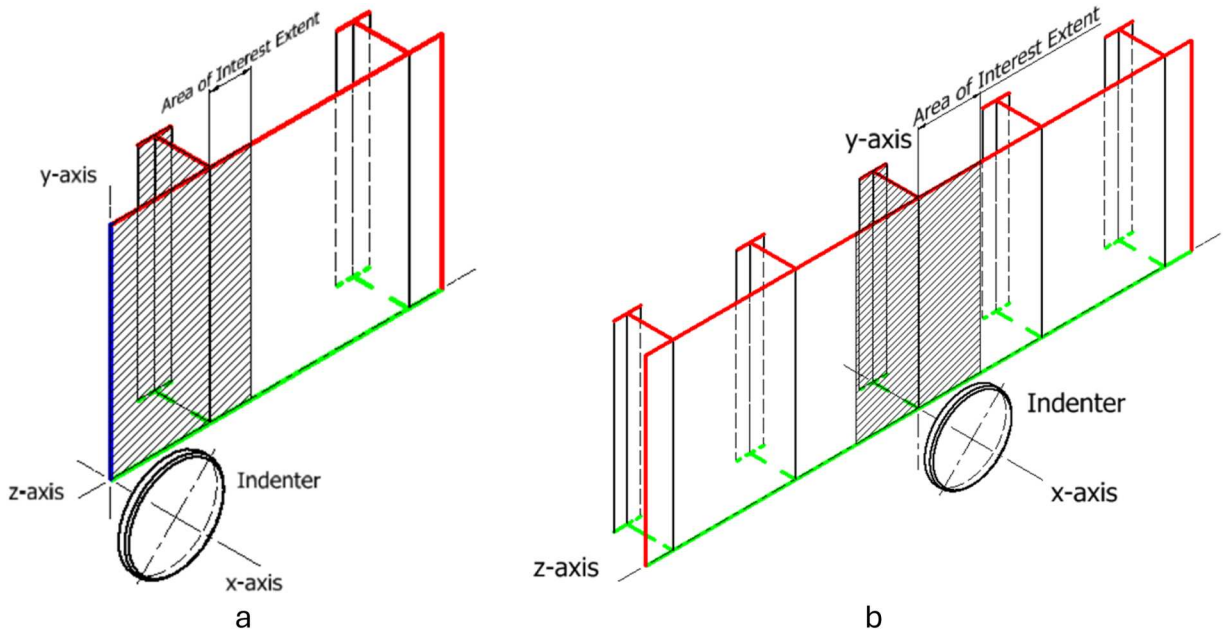

Figure 4. Impact loading setups: (a) original grillage, (b) adjusted grillage. Blue and green represent symmetry; red represents fixed boundary conditions; the hatching indicates refined mesh. (This figure is available in colour online.)

All simulations were terminated when the equivalent plastic strain $\bar{\varepsilon}_p$ surpassed 1.5, and no damage softening or fracture was implemented. This allowed for the state of strain to be analyzed up to and including very ductile materials. When damage is implemented and element deletion occurs, this causes the simulations to be more dominated by the effect of the stress concentrations ahead of a crack rather than extreme deformation. Monitoring simulations with extreme elongations alternatively offers the chance to monitor the behavior of various zones in the grillage when subjected to extreme deformation. This shift in the zone of maximum deformation within the grillage occurs as the load is continuously applied and the resistance to the loading from the grillage is shifted from one zone to another. Nevertheless, it should also be mentioned that it is also possible to postprocess the same results obtained from those simulations using any uncoupled damage model in a future study if different aims are targeted.

2.3. Loading scenarios

The stiffened panels were subjected to a variety of loading conditions to observe their response to extreme conditions. The loading scenarios are intended to form a set of generic cases that cover a variety of different loading types rather than specific design conditions. The loading scenarios can be broadly grouped into two categories: blast loading and impact loading. Each scenario was simulated using two materials (which will be introduced in section three) and utilizing both shell elements and solid elements in different simulations.

2.3.1 Blast loading scenarios

For simulating blast loading scenarios, an air-blast incident wave with a point source was introduced using the Abaqus CONWEP charge interaction property at different conditions for each case. The setups for those scenarios are illustrated in Figure 3. The surfaces highlighted in green denote symmetry about the x-z plane while the surfaces highlighted in blue denote symmetry about the x-y plane. The surfaces denoted in red denote fixed boundary conditions where all six degrees of freedom are constrained. For the solid simulation, the hatched regions in Figure 3 represent the area of interest with the finer mesh while outside it is the coarse mesh.

Different conditions were then used to simulate different scenarios. Those conditions can be summarized in Table 1. The location of the blast source and the quantity of equivalent TNT were always chosen to be theoretically sufficient for the maximum equivalent plastic strain to reach 1.5 in the simulations.

For scenario one, the blast occurred opposite an unsupported portion of the plate and the area of interest extended beyond the first stiffener. For the second scenario, both the blast source and the blast distance were chosen to simulate a pressure wave affecting the whole grillage. The blast source was hence chosen such that the difference between the distances between the source and any point along the impacted surface of the plate

Table 2. Impact loading scenarios.

Scenario	Grillage	Symmetry condition	Impact location	Indenter diameter (*mm*)	Area of interest extent (*mm*)
1	original	quarter	unsupported	304.8	32
2	original	quarter	mix	700	91.95
3	original	quarter	mix	1080	312
4	adjusted	half	stiffener	304.8	232

was within 5%; of each other. Due to the nature of the pressure wave affecting almost all parts of the plate simultaneously, the full grillage was therefore simulated using a fine mesh. The blast source for both scenarios was on the x-axis. For scenario three, the adjusted grillage was used to simulate a blast occurring a portion of the plate supported by a stiffener. Due to the presence of a stiffener exactly in the center of the grillage, a one-half symmetry model was used rather than a one-quarter in order to properly simulate buckling. In order to ensure that the buckling of the stiffener occurs in the same direction for all simulations, the blast source was offset by a distance of 16 mm from the x-axis in the positive z-axis direction. The area of interest in this scenario extended on both sides of the central stiffener.

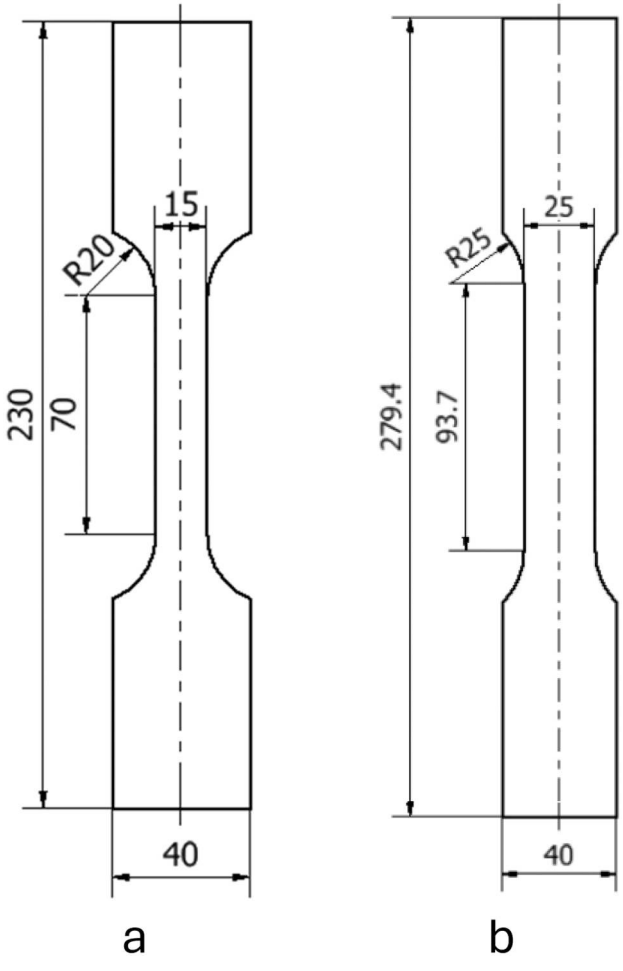

Figure 5. Dogbone specimens: (a) G40 - 2 mm thick, (b) S690 – 6 mm thick (Dimensions in mm). (This figure is available in colour online.)

2.3.2 Impact loading scenarios

For simulating impact loading scenarios, indenters with different sizes were used to impact the grillages. The setups for those scenarios are illustrated in Figure 4. Once again, the surfaces highlighted in green denote symmetry about the x-z plane while the surfaces highlighted in blue denote symmetry about the x-y plane. The surfaces denoted in red denote fixed boundary conditions where all six degrees of freedom are constrained. For the solid simulation, the hatched regions in Figure 4 represent the area of interest with the finer mesh while outside it is the coarse mesh.

The indenters were always simulated as analytical rigid bodies with their center on the x-axis. The indenters always had a velocity of 7.486 m/s and moved along the x-axis to impact the grillage. This velocity was chosen as it represents conditions similar to those of the benchmark study experiments presented in (Quinton et al. 2022). The indenter movement was also constrained such that it can only move along the x-axis. Different indenters and impact locations were used to create different scenarios. Those can be summarized in Table 2.

In the first scenario, the original indenter was used to impact an unsupported part of the grillage away from a stiffener. In the second scenario, a bigger indenter was used such that at the beginning the impact would be on an unsupported part of the grillage but gradually the stiffener supported portion was impacted as well. The third scenario involved an even bigger indenter which was close to the fixed boundary condition at the edge of the plate. The areas of interest between scenarios one and three were gradually increased to reflect this change in the impacted zone. For the fourth scenario, the adjusted grillage was used along with the small indenter to simulate a localized impact only

Table 3. G40 material model parameters.

σ_y	345 MPa
C_1	3807 MPa
C_2	3012 MPa
C_3	0.2604
C_4	0.0332
ε_n	0.2

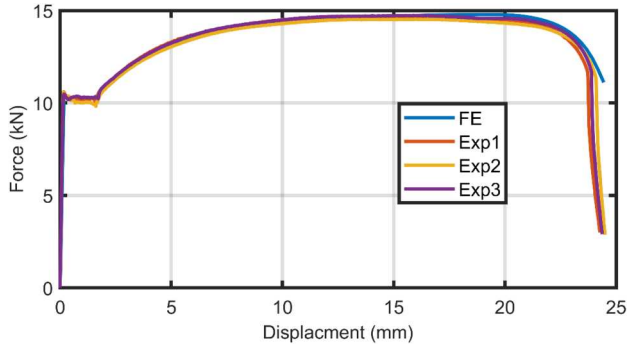

Figure 6. Comparison between FE and experiments for G40 steel. (This figure is available in colour online.)

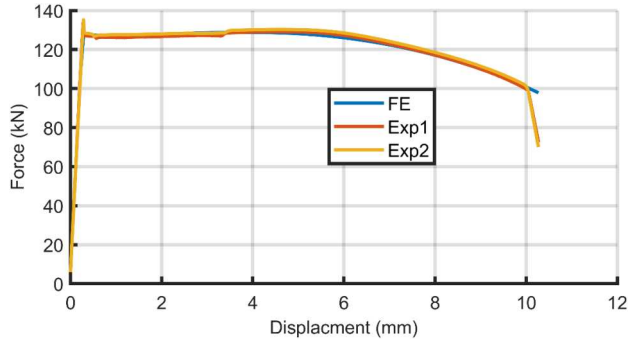

Figure 7. Comparison between FE and experiments for S690 steel. (This figure is available in colour online.)

striking a part of the grillage supported by a stiffener. To properly capture buckling in the central stiffener, only a one-half symmetry model was used. The indenter was also offset by a specified distance16 mm in the z direction to ensure that the stiffener buckling occurs in the same manner for all simulations. The area of interest in this scenario extended on both sides of the central stiffener.

3. Material models

Even though the ISSC ALS benchmark study (Quinton et al. 2022) stiffened grillage was made from CSA G40.21 44W steel, it was also decided to perform additional simulations with S690 QL steel. This was to add some variability in the yield strength to ultimate strength ratios of the simulated cases. The G40 steel is a mild steel with a yield strength to ultimate strength ratio of approximately 0.7 while the S690 steel is high strength steel with a yield strength to ultimate strength ratio of 0.98. As the simulations were run without damage implementations (crack propagation is not the target of this work), no damage modeling was applied for the materials. Standard dogbone tension experiments were used for both materials to obtain plasticity models. For the G40 steel, the experiments were first documented in (Roussel 2021). For the S690, they were first documented in (Wong and Walters 2024) based on sample geometries from (ISO (International Organization for Standardization 2019). The dogbone specimens for both materials are illustrated in Figure 5.

Table 4. S690 material model parameters.

σ_y	857 MPa
A	1057 MPa
n	0.053
C_F	0.05
ε_n	0.053

Both tension experiments were conducted using a servo-hydraulic Instron 88854i axial/torsion machine using a displacement control of 1 mm/min in pure tension. Displacements in the gauge section were measured using Digital Image Correlation (DIC). DIC measurements were taken by two 5 *Megapixel* LIMESS Q400 cameras and Istra4D software was used for postprocessing.

3.1. G40 steel

The elasto-plastic properties for the G40 steel were obtained by running three dogbone specimens under tension. Until the necking point, all the values could be obtained analytically due to the uniformity of the strain in the specimen. After the necking point, an FEA model with 8-node linear brick elements with reduced integration and hourglass control (C3D8R) of 1/8 of the specimen (utilizing symmetry in 3 directions) was used in Abaqus (Dassault Systemes Simulia 2021) to iteratively find a plasticity model that fit the experiments. Four elements were used across the half-thickness of the model.

The elasticity model (obtained from tests) is characterized by an elasticity model $E = 186\ GPa$ and a

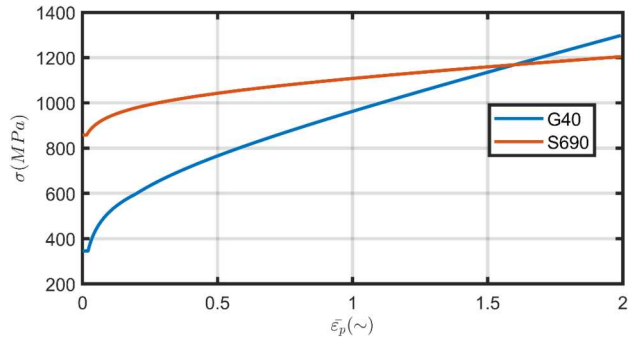

Figure 8. Plasticity models. (This figure is available in colour online.)

Poisson's ratio $\nu = 0.3$. For plasticity, the material was modeled as a von Mises material with the associated flow rule. A modification on the Hollomon power law (Hollomon 1945) was found to work best for this material and can be summarized in Equation (1).

$$\bar{\sigma} = max\left\{ \begin{array}{c} \sigma_y \\ max\left\{ \begin{array}{c} C_1\bar{\varepsilon}^{C_4} - C_2 \\ (C_1\bar{\varepsilon}^{C_4} - C_2)(C_3(\bar{\varepsilon} - \varepsilon_n) + 1) \end{array} \right. \end{array} \right. \quad (1)$$

The von Mises stress is denoted by $\bar{\sigma}$, the equivalent strain by $\bar{\varepsilon}$, the yield stress by σ_y, C_1, C_2, C_3 and C_4 are material-dependent parameters and ε_n is the necking strain. The G40 material parameters are as in Table 3.

The comparison between the three conducted tension experiments and those performed with finite element (FE) using the developed material model on Abaqus can therefore be demonstrated in Figure 6.

3.2. S690 steel

The elasto-plastic properties for the S690 steel were obtained by running two dogbone specimens under tension. Once again, it was possible to obtain all the values for the model analytically until the necking point. After the necking point, the same strategy of utilizing an FEA model of 1/8 of the specimen (utilizing symmetry in three directions) and with the same settings to iteratively find a plasticity model that fit the experiments was used.

The elasticity model (obtained from tests) is characterized by $E = 214\ GPa$ and $\nu = 0.3$. Once again, a von Mises material along with the associated flow rule was used for plasticity. Another modified version of the Hollomon power law (Hollomon 1945) was found to best represent this material and is summarized in Equation (2).

$$\bar{\sigma} = max\left\{ \begin{array}{c} \sigma_y \\ max\left\{ \begin{array}{c} A\bar{\varepsilon}^n \\ (1 + C_F(\bar{\varepsilon} - \varepsilon_n))A\bar{\varepsilon}^n \end{array} \right. \end{array} \right. \quad (2)$$

The new material-dependent parameters are denoted by A, and C_F while n is the strain hardening exponent. The S690 material parameters are therefore as in Table 4.

The comparison between the two tension experiments and with the corresponding finite element (FE) simulation using the material model on Abaqus are shown in Figure 7.

3.3. Summary

Through the FE calibration models, the maximum equivalent plastic strain $\bar{\varepsilon}_p$ observed was approximately 1.1 for the G40 steel and 0.9 for the S690 steel. However, as the objective of this work is to draw conclusions from simulations under high strain without damage implementation, both material models were used to generate plasticity data beyond $\bar{\varepsilon}_p = 1.5$. The accuracy over the extrapolated range after the observed $\bar{\varepsilon}_p$ in the calibration models is therefore theoretically assumed rather than experimentally verified. Even though this might lead to possible inaccuracies in the extrapolated range, this is not expected to lead to any different conclusions regarding identifying the stress and strain patterns or analyzing the difference between solid elements and shell elements, which are the core objectives of this paper. The plasticity data used for input into Abaqus for both materials can be seen in Figure 8. This shows the two cases the materials were chosen to represent, where the G40 steel has a lower σ_y but more significant strain hardening behavior than the S690 steel. It is expected that many steels used in maritime hull structures would exhibit behavior similar to one of the two chosen steels or behavior in between.

4. Results and discussion

Although this work does not directly include damage, the main motivation of the work is to better understand the states of strain in locations where damage is most likely to occur (critical zones). It will be demonstrated throughout this section that a plane strain deformation pattern is predominant for deformations close to the geometric boundaries such as the grillage edges or boundaries between a plate and a stiffener. Shell elements could properly approximate the deformations at those zones. For deformations occurring within a plate, a generalized plane strain deformation pattern dominates after necking initiation. Shell elements were consistently incapable of capturing post-necking deformation behavior.

In order to demonstrate that, the solid element with the maximum shear stress while still satisfying the criterion that $\eta > -0.33$ is first highlighted for every output step or increment. The maximum shear stress criterion was chosen because it is both a very simple criterion with only one calibration parameter and also has been shown to have comparable results to more sophisticated models (Wierzbicki et al. 2005) while the condition that $\eta > -0.33$ ensures that the stress state of the element would lead to damage accumulating at this particular element. As the simulation progresses, different solid elements at different locations satisfy this condition. For brevity and to maintain clear plots, only results for the element with the highest $\bar{\varepsilon}_p$ are plotted when adjacent or non-adjacent elements in the

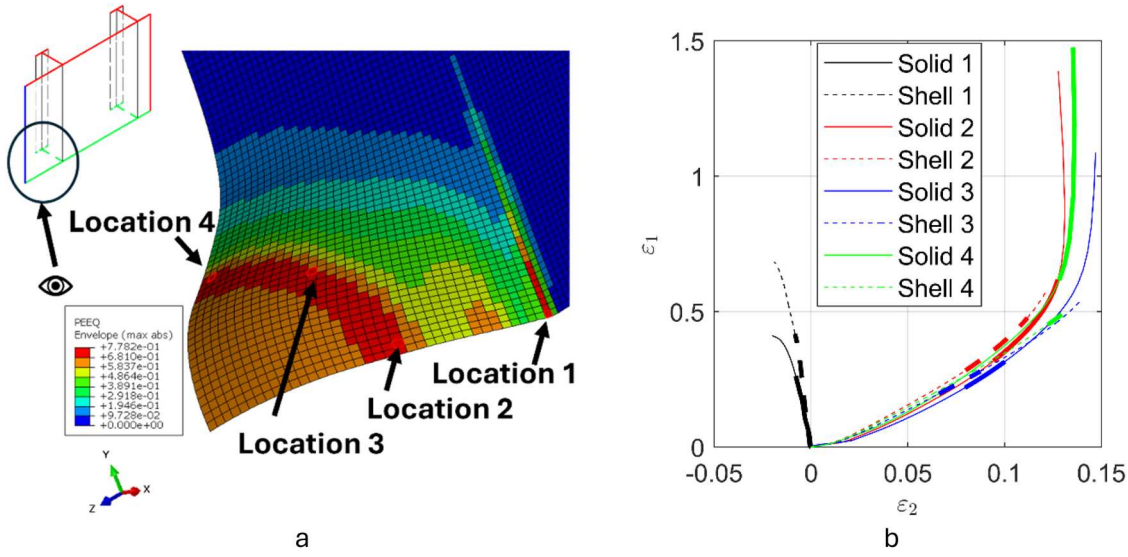

Figure 9. G40 blast opposite plate simulation: (a) Critical zones in shell simulation at termination instant (colors indicate equivalent plastic strain), (b) Principal strain development comparison; bold lines indicate solid element exhibiting maximum shear stress at a particular increment. (This figure is available in colour online.)

same region (same critical zone) show similar behavior. This is not expected to alter the observations or conclusions drawn from the simulations. A comparison will be made between the strain development in each of those elements (at the different critical zones) and the shell element at the same location in the shell simulation. When showing the results in plots, the element exhibiting the maximum shear stress during a particular increment (dominant critical zone) of the simulation was also highlighted through bold lines. As the initial stages of deformation exhibiting low strain values well below those needed to cause necking are not valuable for the purposes of this paper, the solid elements were only considered from the moment the solid simulation exhibited a first principal plastic strain ε_1 equal to the necking strain $\varepsilon_1 = \varepsilon_n$. This condition was chosen as it is a conservative estimate for when the earliest possible point of necking could occur according to (Mu et al. 2020). It should also be noted here that, apart from the fillet in the solid model, no attempt was made to model the weldments, including residual stresses and heat affected zones. While this has no effect when the elements away from the weldments are considered, it should be noted when the results of elements directly at the expected weldment locations (such as at the geometric boundary between the plate and the stiffener) are considered. It should be noted that the simulations with solid and shell elements were not run on the same computers nor with the same number of compute cores, so the simulation times could not be directly compared

4.1. Blast loading scenarios

4.1.1 Blast opposite plate

4.1.1.1 G40 steel. When a blast occurred opposite an unsupported plate in the G40 steel grillage, the strain patterns in the critical zones were as shown in Figure 9.

At the beginning, the critical zone was location one at the boundary between the plate and the stiffener. At this location, an approximately plane strain deformation pattern was observed. The shell element exhibited a higher strain than the solid element, but this is thought to be due to the effect of the fillet in the solid grillage reducing the stress concentrations there. When the deformation evolved, the critical zone moved to locations 2, 3 and 4 which exhibited remarkably similar deformation patterns. All three locations are within the plate and away from any geometric boundary. Even though the second principal plastic strain ε_2 cannot be considered negligible in this case, it is still minimal compared to the first principal strain (always less than 20%; at the end of the simulation). Another important observation can be made regarding the share of the ε_2 component in the straining of the material as deformation progresses. This can be monitored through the slope of ε_2 over ε_1 at any particular increment of the simulation $d\varepsilon_2/d\varepsilon_1$. At a certain point in the simulation shortly following necking initiation, $d\varepsilon_2/d\varepsilon_1$ gradually diminishes until it almost ceases. The necking nearby location four in the solid grillage at the termination instant and the deformation of the shell grillage at the same instant and location in comparison are shown in

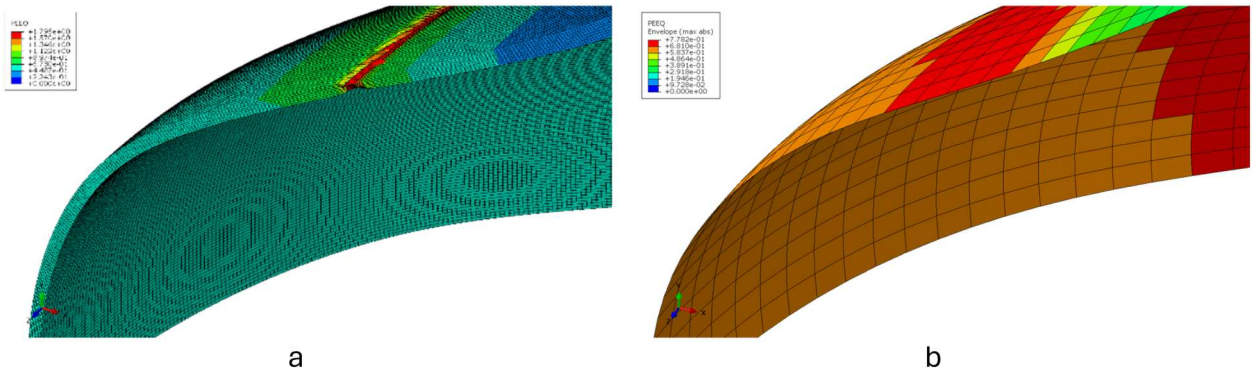

Figure 10. Deformation around location four at the termination instant (colors indicate equivalent plastic strain): (a) Solid grillage showing necking with the critical element highlighted, (b) Shell grillage. (This figure is available in colour online.)

Figure 10. For the sake of brevity, other solid element models are not shown.

This indicates that the deformation could be said to be following a generalized plane strain pattern at that point. In all three locations, the shell elements were incapable of reflecting the strains observed in the solid elements and severely underestimated them.

4.1.1.2 S690 steel. In the same scenario, when the S690 steel grillage was used, the strain patterns were as shown in Figure 11.

It is worthwhile to note that only one critical zone was observed when the S690 grillage was used. As the S690 steel exhibits a lower necking strain than the G40 steel, strain localization at one location occurred without the critical zone changing. This critical zone was once again at the boundary between the plate and the stiffener and with a plane strain deformation pattern occurring, the second principal strains being negligible compared to the first. In this case, the shell element underestimated the strain reflected by the solid element (the ε_1 value exhibited by the shell element was only 68%; that exhibited by the solid element). Two factors were working against each other in this case, while the shell element model did not contain a fillet leading to higher stress concentrations, the excessive localization (and the presence of necking) in the solid element could not be captured by the significantly larger shell elements

4.1.2 Pressure wave

4.1.2.1 G40 steel. The pressure wave impacting the G40 grillage resulted in the strain patterns shown in Figure 12.

All three critical zones were at the external edges of the grillage with negligible second principal strains and therefore plane strain deformation patterns. In all

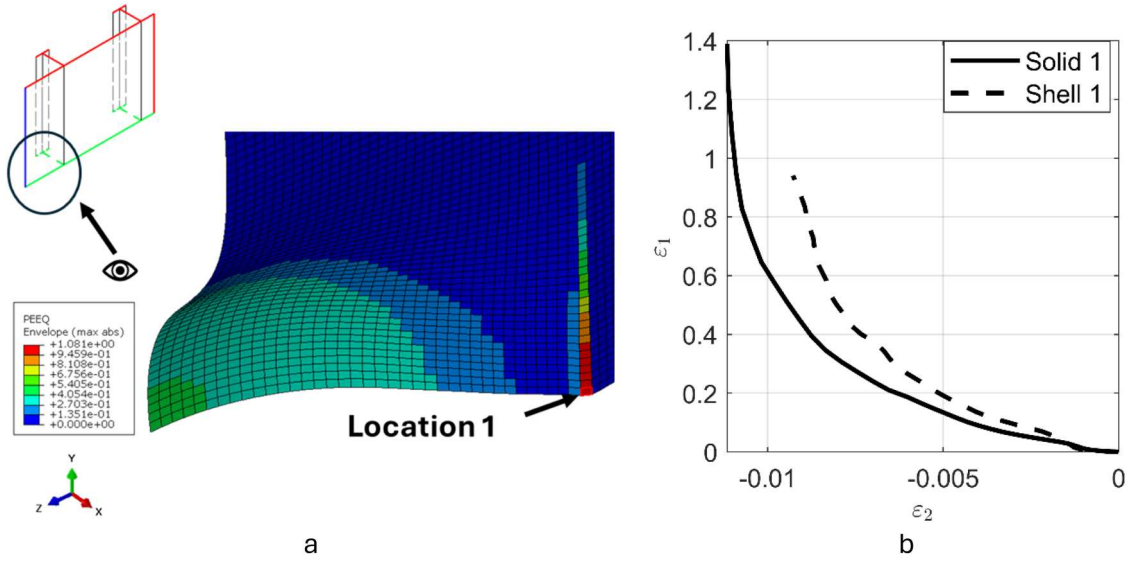

Figure 11. S690 blast opposite plate simulation: (a) Critical zone in shell simulation at termination instant (colors indicate equivalent plastic strain), (b) Principal strain development comparison. (This figure is available in colour online.)

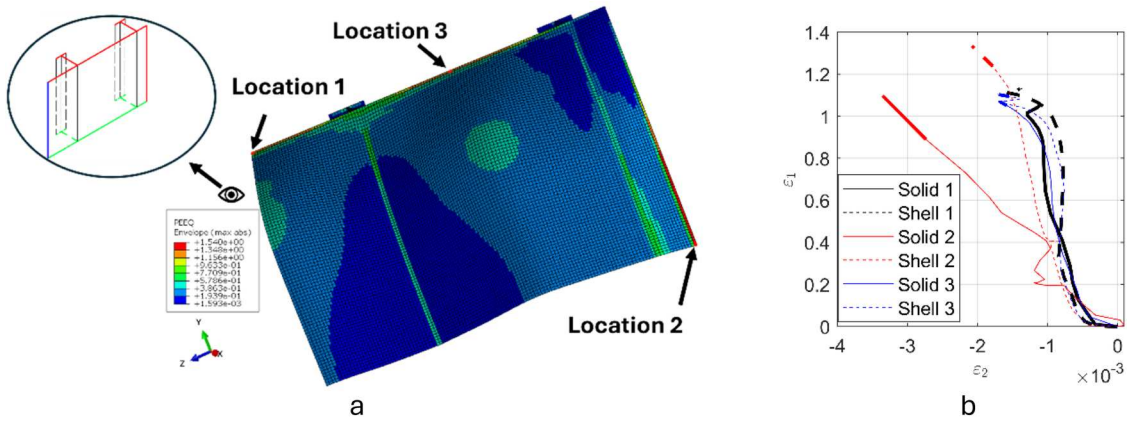

Figure 12. G40 pressure simulation: (a) Critical zones in shell simulation at termination instant (colors indicate equivalent plastic strain), (b) Principal strain development comparison; bold lines indicate solid element exhibiting maximum shear stress at a particular increment. (This figure is available in colour online.)

three locations, the shell elements exhibited approximately the same strains with even a slight overestimation in location two. The three locations were dominated by bending strain, and it should be noted that in location two only the most extreme (and hence the picked one) integration point exhibited strains larger than the solid element. For the solid elements, there was no significant necking development, as necking was still in the very preliminary stages, and the strains were predominantly due to bending stresses.

4.1.2.2 S690 steel. When the S690 grillage was subjected to the same pressure wave, the resulting strain patterns were as shown in Figure 13.

Similar to the G40 simulation, the critical zones were once again all located at the external boundary of the grillage, albeit strictly at the upper edge this time. Plane strain deformation occurred at all locations with negligible second principal strain components. The shell elements could not match the solid elements as well as the G40 case because, in this case, there was a significantly pronounced and developed neck in the solid simulations. The necking strains dominated the bending strains at the critical locations leading to this mismatch. The shell elements continued to only exhibit the bending strains without capturing the necking at all.

4.1.3 Blast opposite stiffener

4.1.3.1 G40 steel. The near blast occurring opposite the stiffener mostly resulted in compressive states of stress to the extent that when $\bar{\varepsilon}_p$ passed a value of 2 in the grillage, the highest $\bar{\varepsilon}_p$ in the grillage with $\eta > -0.33$ was just over a value of 1. It was not deemed realistic to run the models beyond an $\bar{\varepsilon}_p$ value of 2 as this is far beyond the validity of the experiments used to determine the material models. Even though the tension in this case did not reach the threshold value of 1.5, it was decided to present it as a value above 1 is still relevant. The resulting strain patterns are shown in Figure 14.

As the blast was directly opposite the stiffener, only one critical zone existed directly at the border between the plate and the stiffener. The deformation pattern was a plane strain deformation pattern with a negligible second principal strain component. This location was bending dominated with no necking demonstrated. The shell elements slightly underestimate the strains shown by the solid elements. The solid elements localize more, but on the other hand, the shell grillage model does not contain a fillet to relieve stress concentration.

4.1.3.2 S690 steel. The same phenomena that occurred in the G40 grillage occurred in the S690 grillage when it was subjected to a blast opposite the stiffener. An $\bar{\varepsilon}_p$ value in compression reached 2 while the maximum $\bar{\varepsilon}_p$ in elements with $\eta > -0.33$ was just over 1. The resulting strain patterns are shown in Figure 15.

All three critical zones were once again at the boundary between the plate and the stiffener with negligible second principal strains and hence plane strain deformation patterns. The strains were bending strains without any necking in the solid elements. The shell elements reflected almost half the strains in the solid elements where the shell grillage model did not contain a fillet but still could not reflect the strain localizations in the solid elements.

4.2. Impact loading scenarios

4.2.1 Small indenter impacting plate

4.2.1.1 G40 steel. The small indenter impacting the G40 grillage resulted in strain patterns as seen in Figure 16.

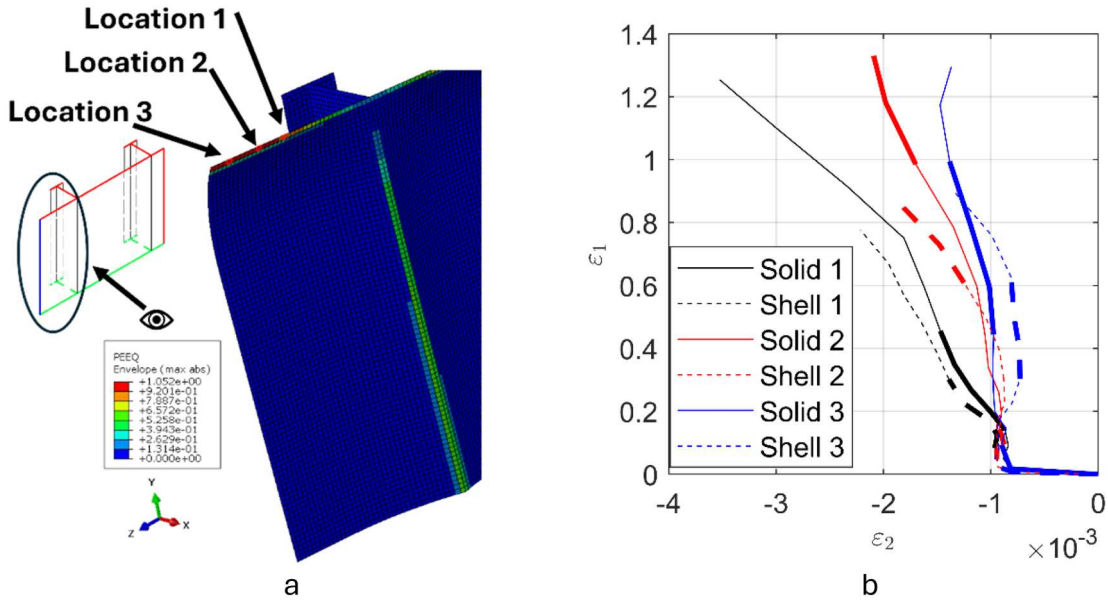

Figure 13. S690 pressure simulation: (a) Critical zones in shell simulation at termination instant (colors indicate equivalent plastic strain), (b) Principal strain development comparison; bold lines indicate solid element exhibiting maximum shear stress at a particular increment. (This figure is available in colour online.)

Location two was only a critical zone at the very early deformation stages which is why the attention could be focused on location one in the analysis. Location one only exhibited relevant $d\varepsilon_2/d\varepsilon_1$ values prior to necking strains. Until necking initiation, the shell elements could capture the strains reflected by the solid elements. Once necking initiated, the $d\varepsilon_2/d\varepsilon_1$ values diminished in the solid element reflecting a generalized plane strain deformation pattern and the shell elements severely underestimated the ε_1 values seen in the solid elements. The necking around location one at the termination instant in the solid grillage and the deformation of the shell grillage at the same instant and location, in comparison, are shown in Figure 17. For the sake of brevity, other solid element models are not shown.

4.2.1.2 S690 steel. When the S690 grillage was impacted with the same small indenter, the strain patterns were as shown in Figure 18.

The S690 results demonstrated qualitatively similar patterns to the G40 results. First, the critical zone was at location two which exhibited considerable $d\varepsilon_2/d\varepsilon_1$ values. However, this was only a critical zone at very initial deformation stages. When the

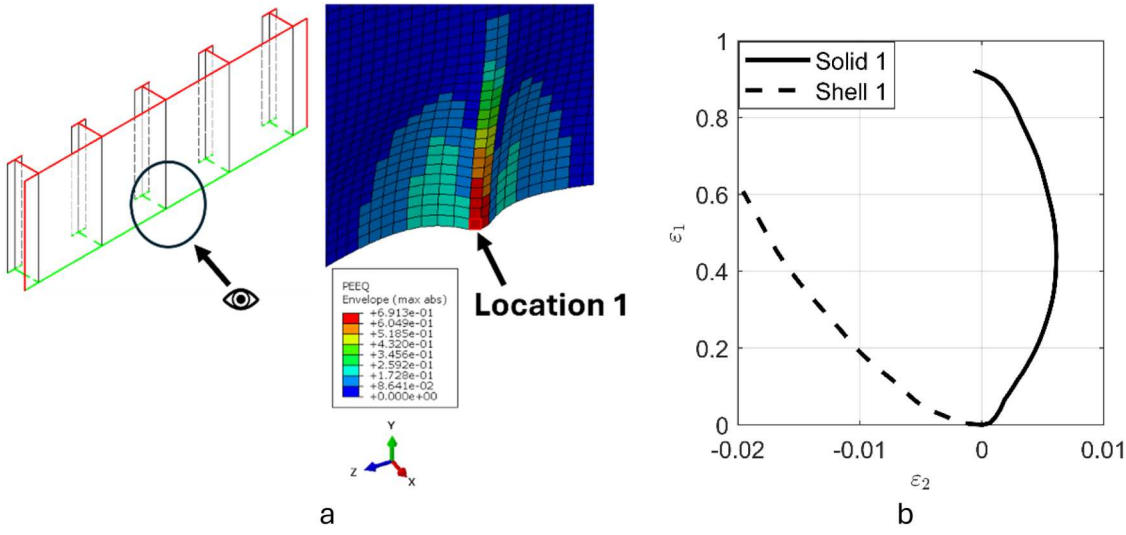

Figure 14. G40 blast opposite stiffener simulation: (a) Critical zone in shell simulation at termination instant (colors indicate equivalent plastic strain), (b) Principal strain development comparison. (This figure is available in colour online.)

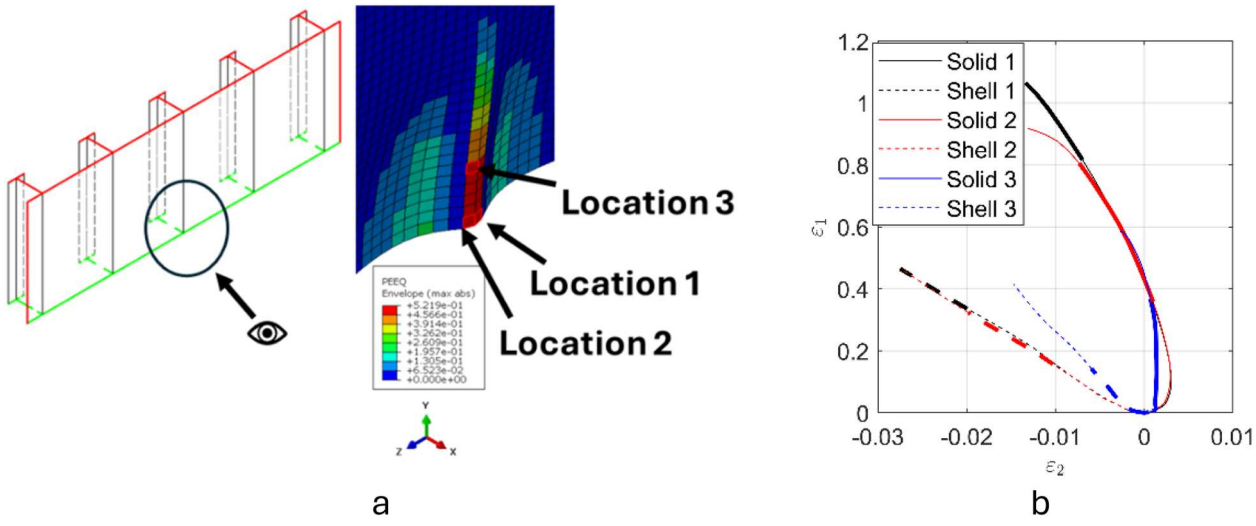

Figure 15. S690 blast opposite stiffener simulation: (a) Critical zones in shell simulation at termination instant (colors indicate equivalent plastic strain), (b) Principal strain development comparison; bold lines indicate solid element exhibiting maximum shear stress at a particular increment. (This figure is available in colour online.)

critical zone became at location one afterwards the shell element overestimated the plane strains shown by the solid elements due to the presence of a stress concentration and the absence of the fillet. The critical zone can, however, be said to have been predominantly at location three within the plate. Considerable $d\varepsilon_2/d\varepsilon_1$ values were only present before necking initiation, and after necking initiation, a generalized plane strain state dominated in the solid element. The shell elements were incapable of capturing the strains at this location.

4.2.2 Medium indenter impacting plate

4.2.2.1 G40 steel. The medium indenter impacting the G40 grillage resulted in strain patterns as shown in Figure 19.

At the beginning of the deformation, the critical zone was at location one at the boundary between the plate and stiffener. At this location and at the beginning of deformation when this location is critical, the values of ε_2 are minimal and the deformation could be said to approximately follow a plane strain pattern. When the critical zone moves to locations three and four at the external boundary of the grillage, the shell elements could approximate the strains shown by the solid elements with the deformation patterns being of plane strain deformation. In the solid grillage, the main strain localization (critical zone) occurs at location two. There are considerable $d\varepsilon_2/d\varepsilon_1$ values only at the beginning, prior to necking initiation, which post-necking moves to a generalized plane strain deformation pattern. The shell element was incapable of capturing the strains at this location due to the presence of necking. It is worth noting that in this scenario, the shell simulation and solid simulation would have exhibited different crack and fracture locations due to the inability of the shell simulation to capture necking localization and thus the deformation is concentrated in a different location. It is also worth explaining why as the critical zones move to locations three and four and afterwards two, high $d\varepsilon_2/d\varepsilon_1$ values are observed at location one. This is due to the fact that as the stiffener totally bends and ceases providing support when the indenter is directly applying deformation at the stiffener, the main deformation direction of elements along the boundary between the plate and the stiffener becomes vertical (in the direction of ε_2). The shell elements at this location show an overestimation of the strains of around 85%; for ε_1 due to the lack of a fillet and stress concentrations

4.2.2.2 S690 steel. The strain patterns for the S690 grillage impacted by the medium indenter are as shown in Figure 20.

In all three critical zones, plane strain deformation patterns were observed with negligible second principal strain. For the solid simulation, the critical zone at the beginning is at location one closely followed by location two near the boundary between the plate and the stiffener. At location one, slightly removed from the boundary, the solid element reflects more strains than the shell element while the situation for location two exactly at the boundary is reversed. The shell element showed significantly more strain than the solid element once again

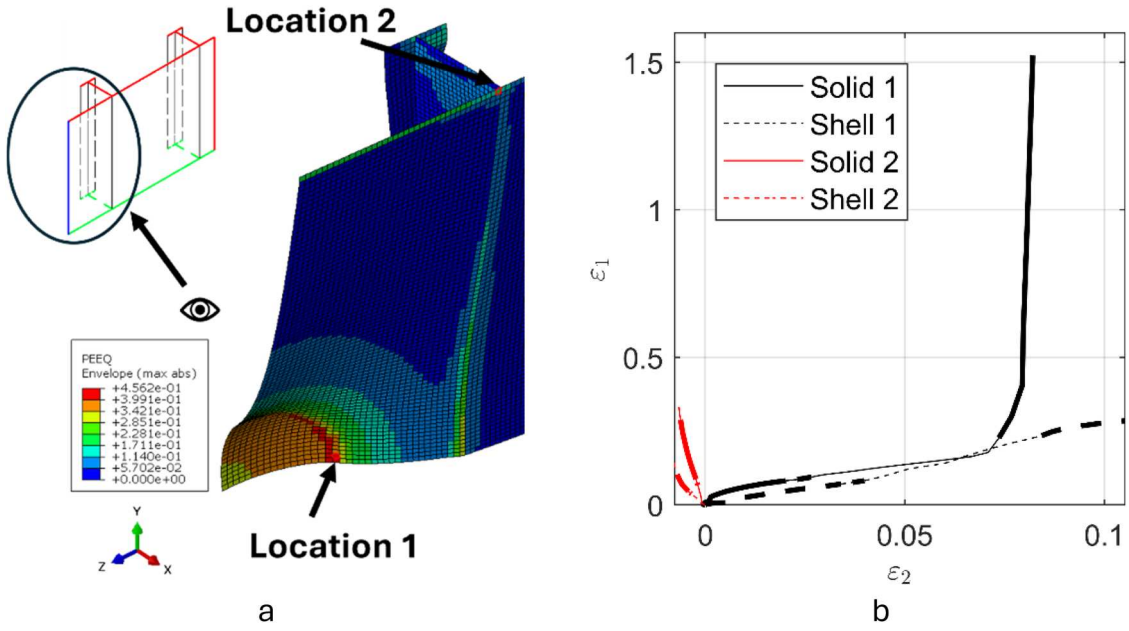

Figure 16. G40 small indenter simulation: (a) Critical zones in shell simulation at termination instant (colors indicate equivalent plastic strain), (b) Principal strain development comparison; bold lines indicate solid element exhibiting maximum shear stress at a particular increment. (This figure is available in colour online.)

due to the stress concentration at the corner. It should also be noted that a degree of necking occurred in the solid simulation adjacent to the stiffener which led to the localization there rather than exactly at the boundary between the stiffener and the plate. Moreover, location two would show the highest strains in the shell simulation. The critical location in the solid simulation eventually moved from location two to three at the external edge of the grillage. The solid element is exhibiting more straining than the shell element due to its ability to simulate necking in contrast to the shell element. The issue that eventual crack formation and failure would appear at distinct locations in both the solid and shell simulations persists in this scenario.

4.2.3 Large indenter impacting plate

4.2.3.1 G40 steel. The large indenter impacting the plate in the G40 grillage resulted in strain patterns at the critical zones as shown in Figure 21.

With the exception of location one, which was the critical zone only at the beginning of the simulation where no considerable damage is expected to occur, the deformation patterns in all the other locations can be said to have been approximately plane strain patterns with very low $d\varepsilon_2/d\varepsilon_1$ values. A significant divergence

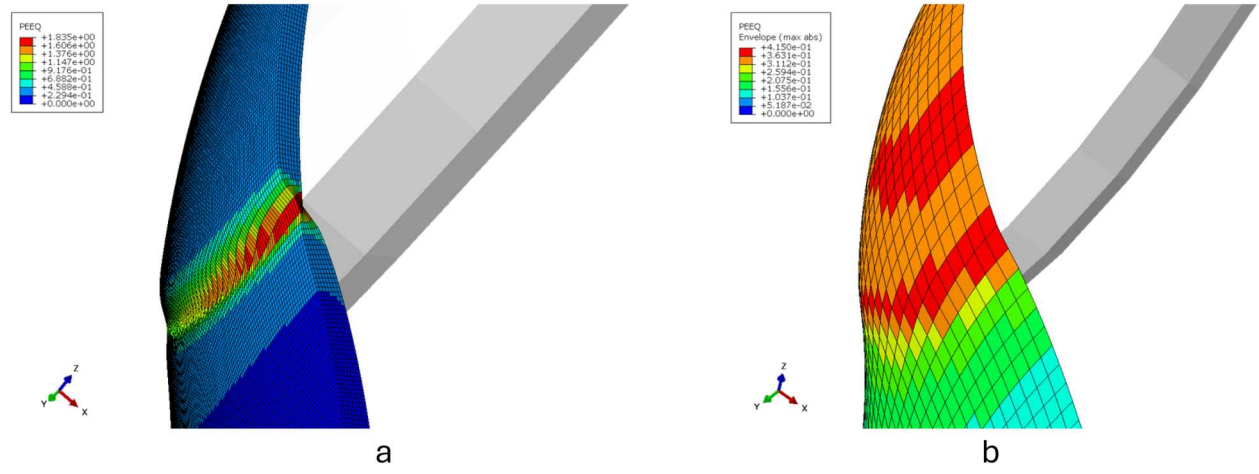

Figure 17. Deformation around location one at the termination instant (colors indicating equivalent plastic strain): (a) Solid grillage showing necking with the critical element highlighted, (b) Shell grillage. (This figure is available in colour online.)

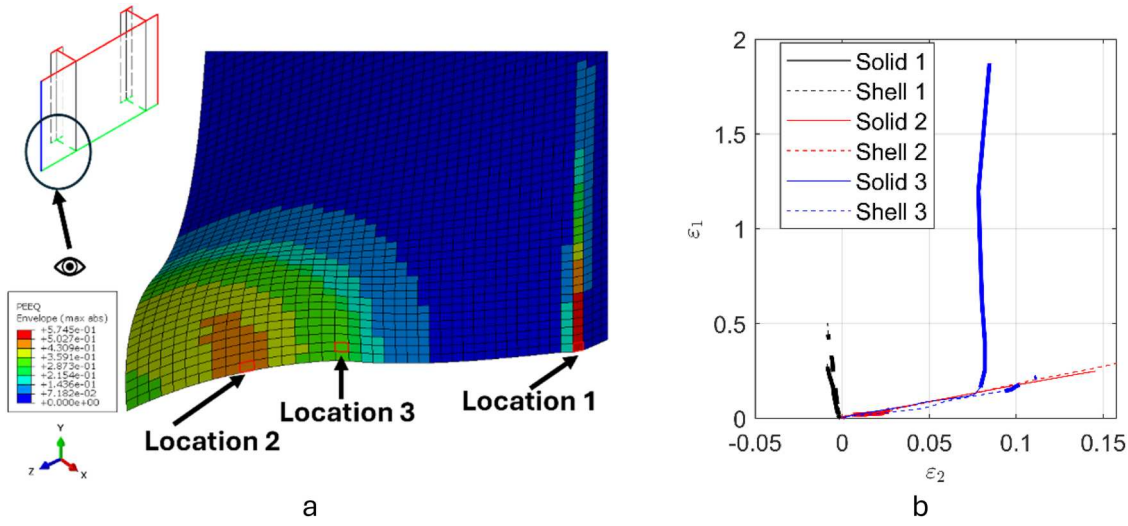

Figure 18. S690 small indenter simulation: (a) Critical zones in shell simulation at termination instant (colors indicate equivalent plastic strain), (b) Principal strain development comparison. (This figure is available in colour online.)

between the solid grillage and the shell grillage occurred regarding where the critical zone was located. In the solid simulation, the critical zone was initially at the boundary between the plate and the stiffener (locations 1 and 3). At these locations, the shell elements closely approximated the same deformations. Later, when the critical zone in the solid simulation moved to location four at the exterior edge of the grillage, the shell elements overestimated the strains at the same location. Moreover, this was the location where the most strain occurred in the shell grillage. When the critical zone became location two within the plate for the solid grillage, this was not captured by the shell grillage, where no significant straining had occurred at this location. This means that a diversion would have occurred between the shell simulation and the solid simulation with regards to where cracking and failure would occur. This stemmed from the fact that the shell simulation was once again incapable of capturing strain localizations within the plate.

4.2.3.2 S690 steel. The same scenario using the S690 grillage resulted in strain patterns as shown in Figure 22.

Once again, for all the critical zones where straining that could lead to significant damage occurred (locations 2, 3 and 4), the deformation patterns can be said to follow a plane strain pattern with the second principal strain negligible compared to the first. Locations 2 and 4 were the critical zones at the beginning of the deformation and followed the same patterns as both are in the vicinity of the boundary between the plate and the stiffener. In both cases, the shell elements overestimated the strain exhibited by the solid elements which is once again thought to be due to the lack of a fillet at this location. Moreover, this is the location where the maximum strain was expected to occur in the shell simulation in contrast to location three in the solid simulation. For the solid simulation, the strain localized significantly at location three. At location three at the external edge of the grillage, necking started to occur in the solid simulation which was not captured by the shell simulation. This would once again probably lead to a divergence between the solid and shell simulation regarding where cracking and fracture would occur.

4.2.4 Small indenter impacting stiffener

4.2.4.1 G40 steel. The resulting strain patterns from the small indenter impact in this scenario are shown in Figure 23.

The critical zone at the beginning was at location three where only strains smaller than those needed to initiate necking in the solid element were demonstrated. The shell element once again overestimated the strains at this location die to the lack of a fillet. However, this location can be disregarded in the analysis as it was only relevant at the very initial deformation stages and was overshadowed by locations one and two. The results for locations one and two are particularly interesting where it can be considered that they are both qualitatively remarkably similar with location one quantitatively exaggerating the same trends observed in location two. In the solid simulation, both locations initially exhibit deformations dominated by ε_1. When ε_1 has achieved around 80%; of its final value, ε_2 was 14% of ε_1 for location two and 21% for location one. Toward the end of the simulation, however, the deformation is almost strictly in the second principal strain

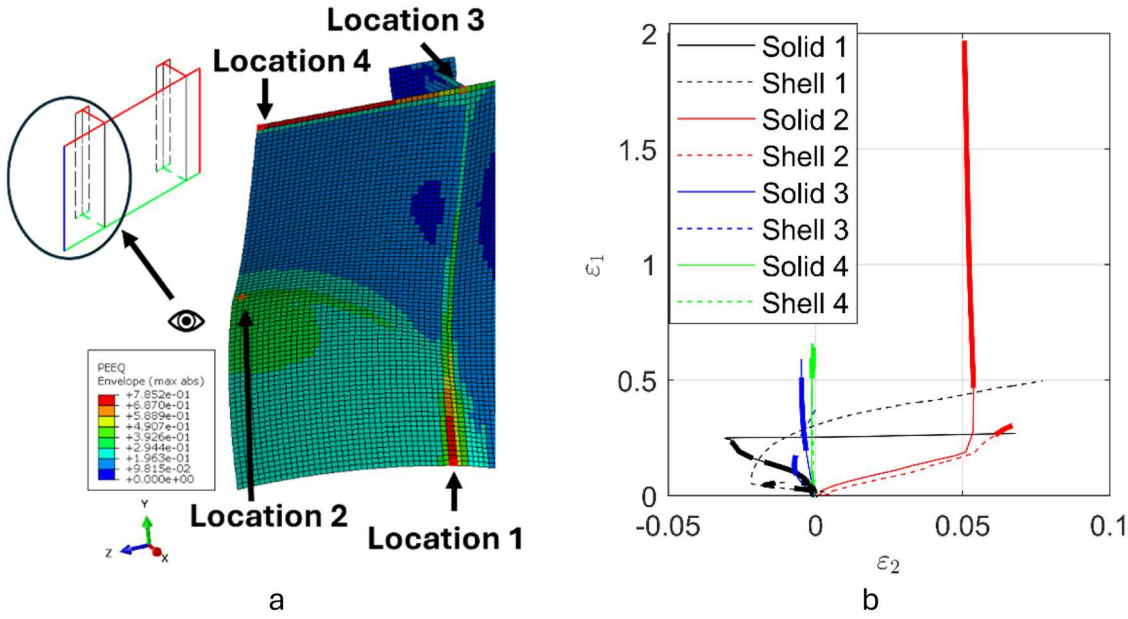

Figure 19. G40 medium indenter simulation: (a) Critical zones in shell simulation at termination instant (colors indicate equivalent plastic strain), (b) Principal strain development comparison; bold lines indicate solid element exhibiting maximum shear stress at a particular increment. (This figure is available in colour online.)

with very high $d\varepsilon_2/d\varepsilon_1$ values. This can be evidenced by the fact that at the end of the simulation ε_2 was 19% of ε_1 for location two and 39% for location one with this marked increase more perceptible in location one. This occurs as initially both elements are expanding horizontally with the stiffener still providing support. However, as the stiffener fully folds on itself and ceases to provide considerable support, the elements start expanding vertically along with the now folded stiffener. The complex loading paths in this case reflect the complex scenario where the stiffener is fully folded on itself, thus splitting the deformation into two segments prior to that folding and after it. The shell elements in both cases underestimated the strains shown in the solid elements due to their inability to capture the proper localizations.

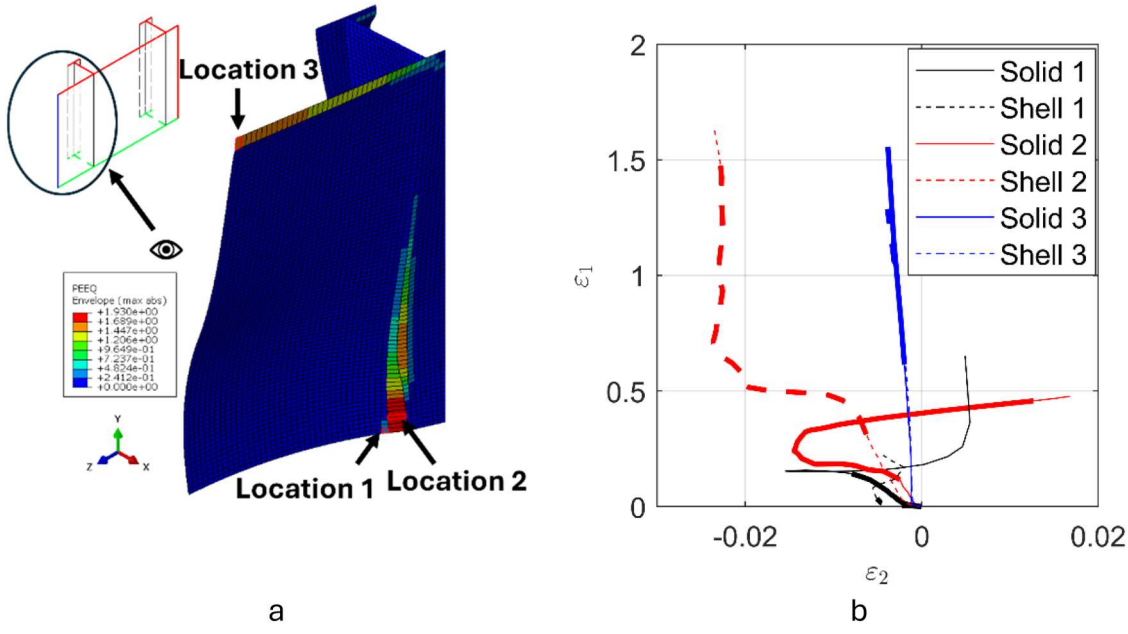

Figure 20. S690 medium indenter simulation: (a) Critical zones in shell simulation at termination instant (colors indicate equivalent plastic strain), (b) Principal strain development comparison; bold lines indicate solid element exhibiting maximum shear stress at a particular increment. (This figure is available in colour online.)

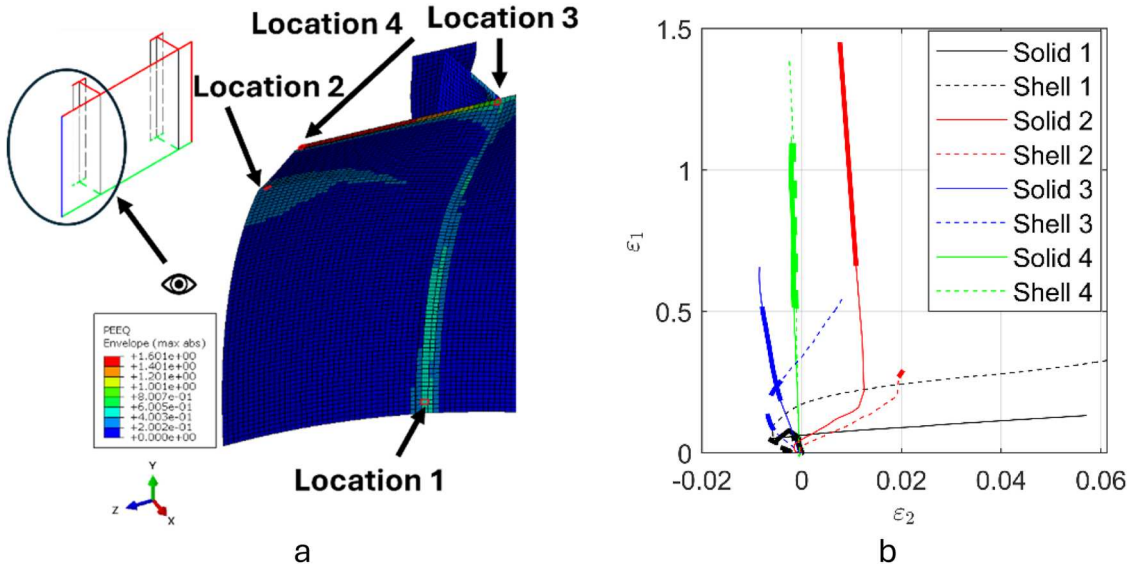

Figure 21. G40 large indenter simulation: (a) Critical zones in shell simulation at termination instant (colors indicate equivalent plastic strain), (b) Principal strain development comparison; bold lines indicate solid element exhibiting maximum shear stress at a particular increment. (This figure is available in colour online.)

4.2.4.2 S690 steel. The results when the same scenario occurred with the S690 grillage are presented in Figure 24 even though the maximum $\bar{\varepsilon}_p$ value for solid elements with $\eta > -0.33$ was just over 0.7 when elements in compressive state had already reached values over 2. This is to demonstrate the particular set of conditions exhibited in this case even though the strain range is below the threshold value expected to signal failure.

First, location two only had miniscule strains (ε_1 less than 0.09 and ε_2 around 0.02) in both the solid and shell simulations, so they can be ignored in the analysis. At location one within the stiffener, an interesting pattern emerged. In the solid element, the element initially was compressing within the stiffener which then transitioned to bending tension when further deformation was applied by the indenter. This can be seen in the plot as the first principal strain increasing (the compression stage) and then appearing to further decrease to zero before increasing again (the tension stage). This was also within a plane strain deformation pattern in both loading directions with negligible second principal

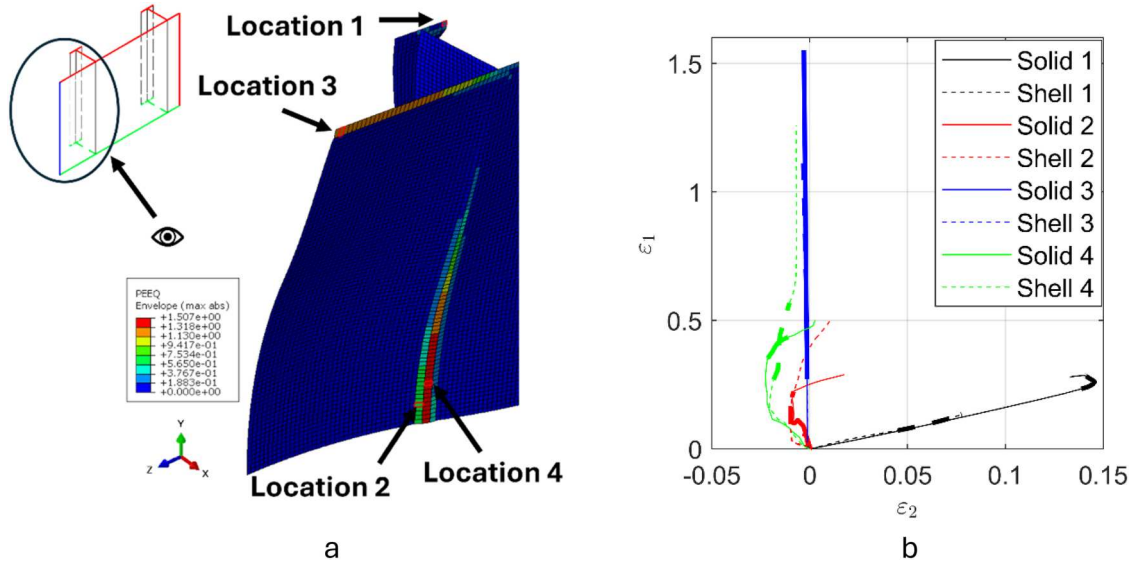

Figure 22. S690 large indenter simulation: (a) Critical zones in shell simulation at termination instant (colors indicate equivalent plastic strain), (b) Principal strain development comparison; bold lines indicate solid element exhibiting maximum shear stress at a particular increment. (This figure is available in colour online.)

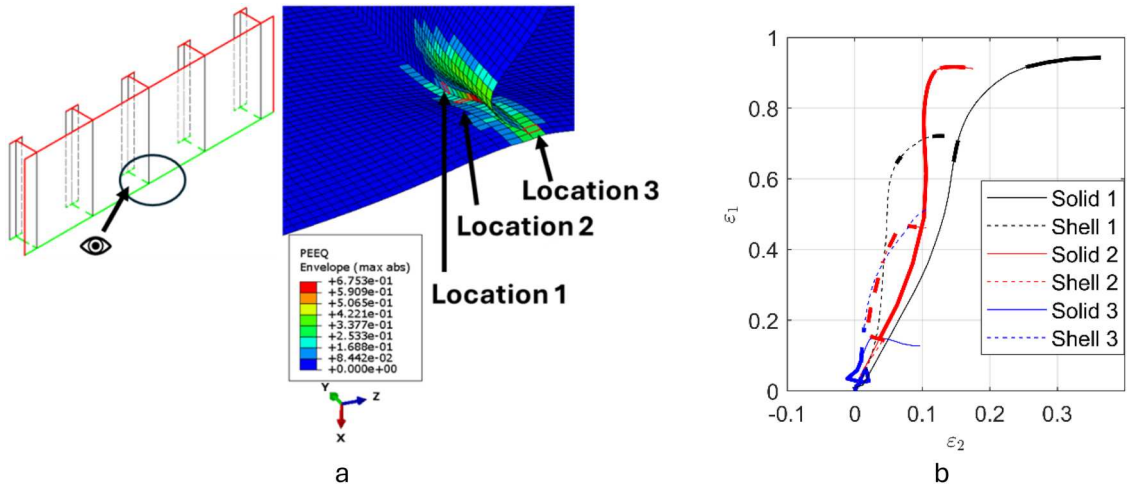

Figure 23. G40 small indenter opposite stiffener simulation: (a) Critical zones in shell simulation at an intermediate step (colors indicate equivalent plastic strain), (b) Principal strain development comparison; bold lines indicate solid element exhibiting maximum shear stress at a particular increment. (This figure is available in colour online.)

strains. The shell element at the same location did not exhibit the strain reversal leading to it eventually overestimating the strain reflected by the solid elements.

4.3. General discussion

First, some simulation choices will be discussed. The aim of this study was to qualitatively assess the states of strain predominant in accidental loading of maritime structure and the degree to which shell simulations can match solid simulations for several scenarios. Therefore, the relative magnitudes of the strains in different directions were far more important than finding the exact values of the stresses and strains in different directions. While a converged mesh would have helped to obtain the exact values, using the non-converged mesh with eight solid elements through the thickness was sufficient for the goals of the study. Furthermore, the decision to use eight solid elements through the thickness was consistent with the computational resources available for this study. Additionally, the characteristic dimension of shell elements of around one times the thickness of the structure was chosen to be between two recent, relevant benchmark studies (Ringsberg et al. 2018; Quinton et al. 2022), reflecting the trend to use shell elements of less size for higher accuracy. Shell elements of a characteristic dimension less than the thickness of the structure are typically not used. The chosen size therefore reflects the most accurate choice within the typically used sizes. The decision to not attempt to model welding details at the geometric boundaries (for example between the stiffener and the plate or at the edges of the grillage) was influential on the results and can even be considered one of the limitations of this study. The presence of a fillet in the solid element grillage and the lack thereof in the shell element grillage led to a difference in the extent of localization of strains at the geometric boundaries and highlights the need to accurately model further details such as heat affected zones and curvatures in the solid simulations to obtain accurate results. This is also a challenge that needs to be explicitly considered in order to make shell element simulations more accurate and representative of realistic scenarios.

Second, in order for the general trends from the simulation results to be discussed, they will be summarized in Appendix A Results Summary. Regarding the strain patterns observed in simulations, it can be conclusively stated that a state of generalized transverse plane strain dominates the deformation patterns at all the critical locations observed. Here, the first principal stress is assumed to be in the plane of the plate, the transverse direction is perpendicular to it in the plane of the plate, and generalized transverse plane strain reflects the assumption that the transverse plane strain remains constant after the onset of necking. The first principal strains were always the dominant driving factor in deformation, and when second principal strains were present, they were limited to certain values and certain locations. Out of the 40 analyzed critical locations, eight locations had both ε_2 absolute values above $0.05\varepsilon_1$ at termination and absolute values of $d\varepsilon_2/d\varepsilon_1$ above 0.05 after ε_1 had reached ε_n. Of those eight locations, this exceptionally considerable value of ε_2 could be attributed in four cases to a change in the loading direction due to the stiffener fully folding and not providing support. In those cases straining occurred at two stages where it can be characterized as generalized plane strain in two perpendicular directions due to the particularities of loading

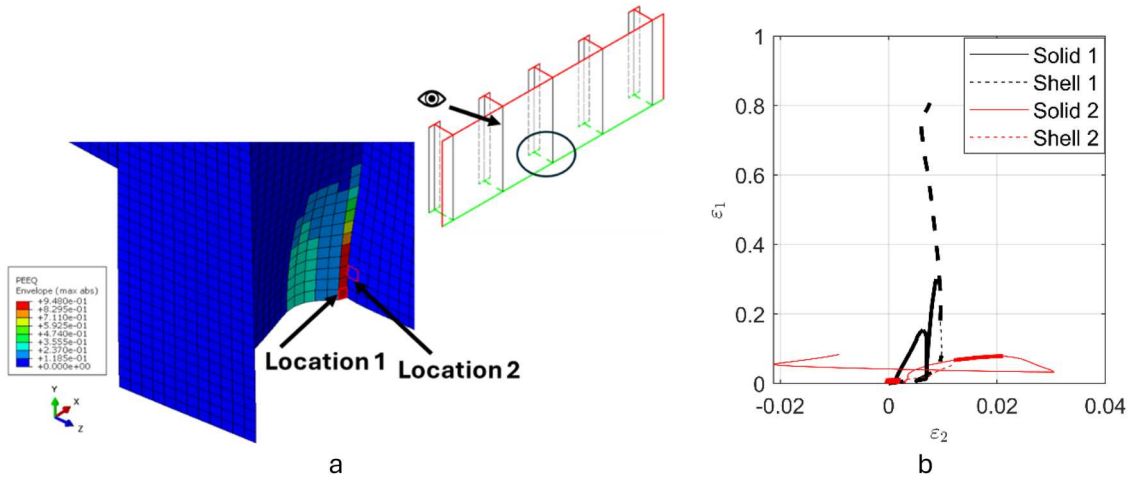

Figure 24. S690 small indenter opposite stiffener simulation: (a) Critical zones in shell simulation at termination instant (colors indicate equivalent plastic strain), (b) Principal strain development comparison; bold lines indicate solid element exhibiting maximum shear stress at a particular increment. (This figure is available in colour online.)

when the stiffener has fully buckled. Three more cases did not have ε_1 demonstrate high values at termination (never passed 0.4) and loading was characterized by multi-axial stress states that would delay necking initiation which is the driver for the strain dominating in the ε_1 direction. The one remaining case where significant necking occurred accompanied by significant ε_2 values had a $d\varepsilon_2/d\varepsilon_1$ value of just 0.08 after ε_1 had reached ε_n and can also be attributed to a delay in necking when multi-axial stress states were present.

Third, strain localization locations will be discussed. The strain primarily localized in three distinct locations depending on the loading scenario and the material of the grillage. When the localization was located within the plate away from the external edges of the grillage or the geometric boundary between the plate and stiffener, the localization was primarily due to membrane stresses and leading to necking within the plate. In this case, second principal strains existed up to the moment of necking initiation, and afterwards, deformation followed a generalized plane strain pattern with a negligible additional second principal strain component. The shell elements were incapable of reflecting the strain localizations demonstrated by the solid elements due to their inability to capture the necking phenomena. This can be evidenced by the fact that out of the ten critical locations where this occurred, in eight of them the shell elements exhibited ε_1a maximum of 0.5 that exhibited by the solid elements and an average of 0.29. The two cases that did not follow this trend were characterized by no neck development and therefore also fit the observation that the shell elements were successful in capturing behavior up to the necking initiation point.

When localization occurred at the geometric boundary between the stiffener and the plate, the results were less conclusive. On one hand, the lack of a fillet in the shell element grillage led to higher stress concentrations there than the solid simulation. On the other hand, the smaller element sizes in the solid simulation led to higher strain localizations. Furthermore, when necking sometimes occurred in those locations, the solid elements would again show higher strain localizations. The interaction between those factors led to the shell element sometimes overestimating the strains shown by the solid elements rather than the expected opposite. This is, however, expected to change when further welding geometric details or heat affected zones are included in the simulations or smaller solid elements closer to the size needed for convergence are used. This highlights the need for further accurate considerations of the welding geometry and heat affected zones for the solid element simulations and the need for methods to account for those factors in the shell element simulations. The strains in those locations were exclusively plane strain deformations with a negligible second principal strain component except when particular loading conditions (such as the stiffener fully folding and the loading direction switching), as discussed earlier, existed.

When localization occurred at the external grillage boundaries where no fillet existed, the results were more conclusive. Deformations at this location were characterized by a high degree of bending stresses with a varying degree of the membrane stress component that leads to necking. When deformation was dominated by the bending stress component, the shell elements could approximate the strain behavior reflected by the solid elements. The shell elements

exhibited a minimum ε_1 of 0.65 that of the solid elements and a maximum of 1.22 exhibiting the closer correlation in this case. The cases that diverged more were the ones associated with a more prevalent necking in the solid simulation. It is also worth mentioning here that even though eight solid elements across the thickness are definitely not mesh convergent when necking occurs, they offer an accurate estimate of strains when strictly bending is involved. For example, when the G40 pressure simulation (dominated by external edge bending without significant necking) using solid elements was conducted with four elements across the thickness rather than eight, the difference in maximum strains was less than 10%. The results at those locations where no necking occurs are therefore expected to change to an even lesser degree if further mesh refinement is done. This supports the conclusion that shell elements were properly approximating the true strains predicted by the solid elements. When a significant strain due to considerable membrane stresses occurred, however, necking sometimes initiated at those locations leading once again to the shell elements' inability to capture the solid element behavior (underestimating it) due to its inability to capture necking. Strains at those locations were also characterized by being in plane strain with a negligible second principal strain.

5. Conclusions and future work

Finally, the results for this study can be summarized in the following points:

- Straining occurring close to the geometric boundaries such as grillage edges or boundaries between a plate and a stiffener follows a plane strain deformation pattern.
- Straining occurring within a plate away from any geometric boundaries usually has considerable first principal and second principal strain components up to the point of necking initiation. From this point onwards, strains follow a generalized plane strain pattern with limited successive straining in the direction of the second principal strain.
- Shell elements were incapable of capturing deformation behavior when necking occurred due to membrane stresses. Therefore, shell elements should not be considered reliable in cases where significant deformation is expected to occur in the plate away from stiffeners and geometric boundaries where necking is expected to occur.
- Shell elements were capable of properly approximating deformation behavior due to bending stresses rendering them more reliable for cases where the deformation is expected to be mostly at stiffeners or geometric boundaries.
- Deformation occurring at geometric boundaries needs accurate geometric details and further considerations of welding details (such as heat affected zones) when present to be accurately predicted.

The suggestions for future work clearly follow the conclusions obtained from this work. It is recommended to focus on developing analytical approaches to account for necking that could be implemented in shell element simulations. This would drastically improve the accuracy of accidental loading simulations while not sacrificing the practicality of the shell elements and their relatively low need for computational power compared to solid elements. For deformations within the plate away from geometric boundaries, necking dominates the higher strains and the fact that this deformation occurs in a generalized plane strain pattern also aids in defining an approach for such an issue. The first priority should therefore be on analytical approaches for accounting for plane strain necking. For deformations occurring at the geometric boundaries, details such as the geometric curvature or heat affected zone information need to be accounted for in the shell element simulation due to the significant effect they have on bending at those locations. This is, however, also an issue that is present in solid simulations. The developed approach for those zones needs to take into account that deformations are strictly plane strain deformations.

Author contributions

CRediT: **Mohammed A. Adly:** Conceptualization, Formal analysis, Investigation, Methodology, Software, Validation, Visualization, Writing – original draft, Writing – review & editing; **Carey L. Walters:** Conceptualization, Funding acquisition, Project administration, Resources, Supervision, Writing – review & editing.

Disclosure statement

No potential conflict of interest was reported by the author(s).

Funding

This work has been done within the FailSafeShip project funded by the Dutch Research Council (NWO grant 17112) and with significant contributions from the Netherlands Organization for Applied Scientific Research (TNO), Femto Engineering and Commando Materieel en IT (COMMIT), Nederlandse Ministerie van Defensie to which we are all highly grateful for their contributions.

Notes on contributors

Mohammed A. Adly is since 2021 pursuing his Ph.D. on the ductile fracture of thin-walled steel structures in the Maritime Transport and Technology department at the Technical University of Delft in the Netherlands. Before that he was awarded his bachelor's and master's degrees in 2017 and 2020 respectively in Mechanical Engineering from Cairo University in Egypt.

Dr. Carey L. Walters is currently an associate professor in the Maritime Transport and Technology section at the Technical University of Delft in the Netherlands. He researches fracture of steel due to extreme loading, e.g. due to overloading at low temperatures, crash, or explosions. From 2009 until 2022, Carey worked at TNO (the Netherlands Organization for Applied Scientific Research), focusing on material failure. From 2004 until 2009, Carey completed his Ph.D. thesis at the Impact and Crashworthiness Laboratory at MIT in high strain rate failure of advanced high strength steels. Prior to his time at MIT, he worked at Sikorsky Aircraft (2000 until 2004), where he simulated crash and ground loads of helicopters.

Data availability

The data that support the findings of this study are openly available in 4TU. Research Data at 'https://doi.org/10.4121/f85e3049-a0b5-48ce-ad04-cdd8a9543044.'

ORCID

Mohammed A. Adly http://orcid.org/0000-0001-5114-9209

References

Alsos HS, Hopperstad OS, Törnqvist R, Amdahl J.. 2008. Analytical and numerical analysis of sheet metal instability using a stress based criterion. Int J Solids Struct. 45(7-8):2042–2055.

American Welding Society Committee on Structural Welding. 2000. Structural Welding Code - Steel (AWS D1.1:2000). 17th Edition.

Atli-Veltin B, Dekker R, Brunner SK, Walters CL. 2016. Wrinkling, fracture, and necking: the various failure modes in maritime crash. In Proceedings of the International Conference on Offshore Mechanics and Arctic Engineering - OMAE. American Society of Mechanical Engineers (ASME). https://doi.org/10.1115/OMAE2016-54148.

Bai Y, Wierzbicki T.. 2008. A new model of metal plasticity and fracture with pressure and Lode dependence. Int J Plast. 24(6):1071–1096.

Bai Y, Wierzbicki T. 2010. Application of extended Mohr-Coulomb criterion to ductile fracture. Int J Fract. 161:1–20

Cerik BC, Choung J.. 2020. Rate-dependent combined necking and fracture model for predicting ductile fracture with shell elements at high strain rates. Int J Impact Eng. 146:103697.

Cerik BC, Lee K, Park SJ, Choung J. 2019a. Simulation of ship collision and grounding damage using Hosford-Coulomb fracture model for shell elements. Ocean Eng. 173:415–432

Cerik BC, Park SJ, Choung J.. 2020. Use of localized necking and fracture as a failure criterion in ship collision analysis. Marine Structures. 73:102787.

Cerik BC, Ringsberg JW, Choung J.. 2019b. Revisiting MARSTRUCT benchmark study on side-shell collision with a combined localized necking and stress-state dependent ductile fracture model. Ocean Eng. 187:106173.

Coppejans O, Werter N. 2022. Discretization challenges in crash simulations: mesh, geometry and failure criterion effects from the energy perspective. In Proceedings of the ASME 2022 41st International Conference on Ocean, Offshore and Arctic Engineering OMAE2022. ASME, Hamburg,Germany.

Dassault Systemes Simulia. 2021. Abaqus 2021 user manual.

Det Norske Veritas. 2010. Design against accidental loads (DNV-RP-C204).

Det Norske Veritas AS. 2013. Determination of structural capacity by non-linear FE analysis methods (DNV-RP-C208).

Hollomon JH.. 1945. Tensile deformation. AIME Trans. 12(4):1–22.

ISO (International Organization for Standardization). 2019. ISO 6892-1: metallic materials – tensile testing – part 1: method of test at room temperature. Geneva.

Kõrgesaar M. 2019. The effect of low stress triaxialities and deformation paths on ductile fracture simulations of large shell structures. Marine Structures. 63:45–64

Liu B, Guedes Soares C.. 2023. Recent developments in ship collision analysis and challenges to an accidental limit state design method. Ocean Eng. 270:113636.

Lu Y, Liu K, Wang Z, Tang W, Amdahl J.. 2022. Development of ductile fracture modelling approach in ship impact simulations. Ocean Eng. 252:111173.

Mohr D, Marcadet SJ. 2015. Micromechanically-motivated phenomenological Hosford-Coulomb model for predicting ductile fracture initiation at low stress triaxialities. Int J Solids Struct. 67–68: 40–55. doi:10.1016/j.ijsolstr.2015.02.024.

Mu L et al. 2020. A theoretical prediction framework for the construction of a fracture forming limit curve accounting for fracture pattern transition. Int J Plast. 129:102706.

Neukamm F, Feucht M, Haufe A, Roll K.. 2008. On Closing the Constitutive Gap Between Forming and Crash Simulation. 10th International LS-DYNA Users Conference; Dearborn; MI, USA. pp. 12-21.

Pack K, Mohr D. 2017. Combined necking & fracture model to predict ductile failure with shell finite elements. Eng Fract Mech. 182:32–51

Prabowo AR et al. 2023. Comparative study of shell element formulations as NLFE parameters to forecast structural crashworthiness. Curved and Layered Structures. 10(1):20220217.

Quinton B et al. 2022. Committee V.1 accidental limit states. In: Proceedings of the 21st International Ship and Offshore Structures Congress (ISSC 2022), volume 2. OnePetro. Vancouver, Canada doi:10.5957/ISSC-2022-COMMITTEE-V-1.

Ringsberg JW et al. 2018. MARSTRUCT benchmark study on nonlinear FE simulation of an experiment of an indenter

impact with a ship side-shell structure. Marine Structures. 59:142–157
Rizzuto E et al. 2018. Committee V.1 accidental limit states. In: Proceedings of the 20th International Ship and Offshore Structures Congress (ISSC 2018) Volume II. IOS Press. Liege, Belgium and Amsterdam, The Netherlands. doi:10.3233/978-1-61499-864-8-1.
Roussel L. 2021. Ductile fracture prediction of CSA G40.21 44W steel based on Modified Mohr-Coulomb model. Delft.
Suominen M, Kõrgesaar M, Taylor R, Bergström M.. 2024. Probabilistic analysis of operational ice damage for Polar class vessels using full-scale data. Structural Safety. 107:102423.
Walters CL.. 2014. Framework for adjusting for both stress triaxiality and mesh size effect for failure of metals in shell structures. Int J Crashworthiness. 19(1):1–12.
Wiegard B, Ehlers S.. 2020. Pragmatic regularization of element-dependent effects in finite element simulations of ductile tensile failure initiation using fine meshes. Marine Structures. 74:102823.
Wierzbicki T, Bao Y, Lee YW, Bai Y.. 2005. Calibration and evaluation of seven fracture models. Int J Mech Sci. 47(4-5):719–743.
Wong WJ, Walters CL. 2024. Effects of strain hardening and the lode dependence of the fracture strain locus on slant fracture in Charpy V-notch impact testing. In: Proceedings of the ASME 2024 43rd International Conference on Ocean, Offshore and Arctic Engineering OMAE2024. The American Society of Mechanical Engineers (ASME). Singapore.

Appendix A. Results summary

In order to discuss the general trends from the results, some indicators will be presented for all the scenarios in Table A1. First it will be indicated at which area of the grillage each location considered a critical zone was located. This can be within the stiffener *S*, at the boundary between the stiffener and the plate *SP*, within the plate *P* or at the external edge of the plate *E*. Then, for each location considered a critical zone, the ratio of ε_2 to ε_1 at the termination instant $\varepsilon_2/\varepsilon_{1t}$ for the solid element will be calculated. When this value is equal or below 0.05 the location will be considered to be deforming in plane strain. When this doesn't apply, $d\varepsilon_2/d\varepsilon_1$ will be calculated for the interval after ε_1 surpasses ε_n to indicate the advanced deformation state post possible necking initiation for the solid element $d\varepsilon_2/d\varepsilon_{1\,pn}$. If the value of $\varepsilon_2/\varepsilon_{1t}$ is below 0.05 then $d\varepsilon_2/d\varepsilon_{1\,pn}$ will be considered not relevant *NR*. The ratio of ε_1 at the shell element to ε_1 at the solid element at the termination instant $\varepsilon_{1sh}/\varepsilon_{1sot}$ will be used to indicate the degree to which the shell elements capture the deformation captured by the solid elements.

Moreover, the maximum displacements of the structures for both the solid and shell simulations after impact at the termination instant are also included in Table A2. It can be easily observed that the maximum deformations for the shell and solid grillage almost match exactly for all the indenter simulations as the indenter had a prescribed velocity and simulations were run for similar timeframes. For the blast simulations, the maximum deformation exhibited by the solid grillage was always slightly more than that exhibited by the shell grillage due to the difference in the way the blast energy was dissipated in both cases.

Table A1. Results summary.

Scenario	Location	Area	$\varepsilon_2/\varepsilon_{1t}$	$d\varepsilon_2/d\varepsilon_{1\,pn}$	$\varepsilon_{1sh}/\varepsilon_{1sot}$
1.1.1	1	*SP*	−0.05	*NR*	1.66
	2	*P*	0.09	0.05	0.42
	3	*P*	0.14	0.08	0.5
	4	*P*	0.09	0.05	0.36
1.1.2.	1	*SP*	−0.01	*NR*	0.68
1.2.1.	1	*E*	0	*NR*	1.06
	2	*E*	0	*NR*	1.22
	3	*E*	0	*NR*	1.03
1.2.2.	1	*E*	0	*NR*	0.62
	2	*E*	0	*NR*	0.65
	3	*E*	0	*NR*	0.7
1.3.1.	1	*SP*	0	*NR*	0.66
1.3.2.	1	*SP*	−0.01	*NR*	0.44
	2	*SP*	−0.01	*NR*	0.5
	3	*SP*	−0.01	*NR*	0.71
2.1.1.	1	*P*	0.05	*NR*	0.19
	2	*SP*	−0.02	*NR*	0.43
2.1.2.	1	*SP*	−0.03	*NR*	1.75
	2	*P*	0.59	0.63	1.17
	3	*P*	0.05	*NR*	0.12
2.2.1.	1	*SP*	0.25	2.85	1.85
	2	*P*	0.03	*NR*	0.17
	3	*SP*	−0.01	*NR*	0.65
	4	*E*	0	*NR*	1.04
2.2.2.	1	*P*	0.01	*NR*	0.34
	2	*SP*	0.04	*NR*	3.45
	3	*E*	0	*NR*	0.83
2.3.1.	1	*SP*	0.43	*NR*	2.47
	2	*P*	0.01	*NR*	0.2
	3	*SP*	−0.01	*NR*	0.85
	4	*E*	0	*NR*	1.24
2.3.2.	1	*S*	0.48	0.42	0.48
	2	*P*	0.06	0.09	1.73
	3	*E*	0.01	*NR*	0.72
	4	*SP*	0	*NR*	2.52
2.4.1.	1	*SP*	0.39	0.4	0.77
	2	*SP*	0.19	0.17	0.51
	3	*SP*	0.77	*NR*	4.05
2.4.2.	1	*SP*	0.03	*NR*	2.69
	2	*SP*	−0.11	0.35	0.614

Table A2. Maximum deformations at termination instant.

	Maximum displacement normalized by thickness of structure (non-dimensional)	
Scenario	Solid grillage	Shell grillage
1.1.1.	44.7	42.2
1.1.2.	25.3	23.9
1.2.1.	41.2	41.1
1.2.2.	8.1	7.9
1.3.1.	5.7	4.8
1.3.2.	4.2	3.6
2.1.1.	33	32.8
2.1.2.	23.6	23.4
2.2.1.	47	46.8
2.2.2.	31.1	30.9
2.3.1.	41.3	41.4
2.3.2.	25.5	25.4
2.4.1.	34	34.1
2.4.2.	2.7	2.8

In addition, the x-deformations for the elements along the z-axis were compared between the solid grillage and the shell grillage for three select cases to highlight the trends in the difference in deformations between the solids and shells. Two representative cases were selected for the original grillage

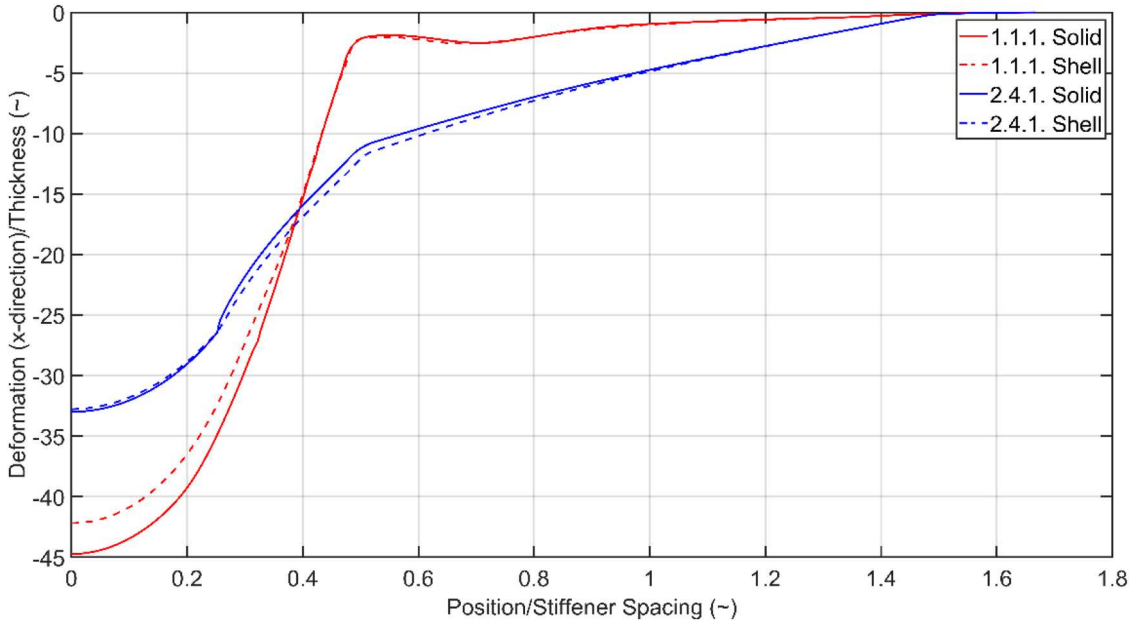

Figure A1. Deformation along the z-axis for an example blast and rigid indenter case on the original grillage.

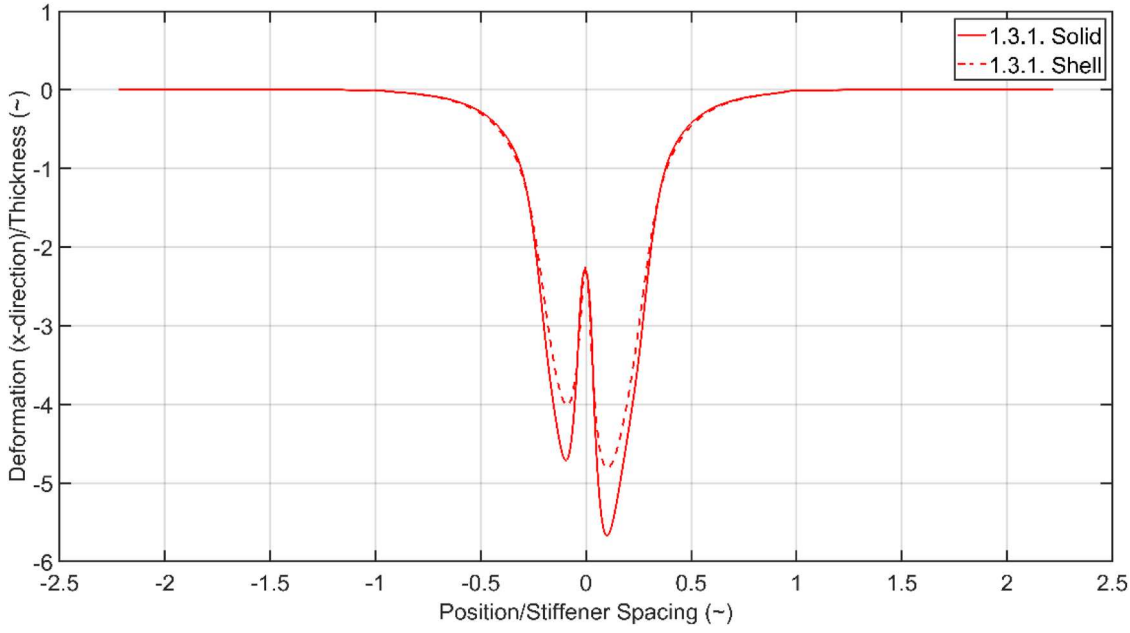

Figure A2. Deformation along the z-axis for a blast case on the adjusted grillage.

and are highlighted in Figure A1. As can be seen, for the blast case (1.1.1), the energy is dissipated differently leading to a difference is deformations from the centre until the first stiffener (present at 0.5 stiffener spacing due to symmetry. For the small indenter (2.4.1), which is representative for all the indenter simulations, as the indenter is moving with a predefined constant velocity the differences are considerably less and can even be said to be negligible in this case.

The case where a blast occurred opposite a stiffener can be seen in Figure A2. Here, a similar trend to the previous blast simulation can be seen, where the blast energy is identical, but it is dissipated differently in the solid and shell grillages.